

# **Evaluation of statistical variation of microstructural properties and temperature effects on creep fracture of Grade 91**

---

**Applied Materials Division**

### **About Argonne National Laboratory**

Argonne is a U.S. Department of Energy laboratory managed by UChicago Argonne, LLC under contract DE-AC02-06CH11357. The Laboratory's main facility is outside Chicago, at 9700 South Cass Avenue, Argonne, Illinois 60439. For information about Argonne and its pioneering science and technology programs, see [www.anl.gov](http://www.anl.gov).

### **DOCUMENT AVAILABILITY**

**Online Access:** U.S. Department of Energy (DOE) reports produced after 1991 and a growing number of pre-1991 documents are available free at OSTI.GOV (<http://www.osti.gov/>), a service of the U.S. Dept. of Energy's Office of Scientific and Technical Information

#### **Reports not in digital format may be purchased by the public from the National Technical Information Service (NTIS):**

U.S. Department of Commerce  
National Technical Information Service  
5301 Shawnee Rd  
Alexandria, VA 22312  
**[www.ntis.gov](http://www.ntis.gov)**  
Phone: (800) 553-NTIS (6847) or (703) 605-6000  
Fax: (703) 605-6900  
Email: **[orders@ntis.gov](mailto:orders@ntis.gov)**

#### **Reports not in digital format are available to DOE and DOE contractors from the Office of Scientific and Technical Information (OSTI)**

U.S. Department of Energy  
Office of Scientific and Technical Information  
P.O. Box 62  
Oak Ridge, TN 37831-0062  
**[www.osti.gov](http://www.osti.gov)**  
Phone: (865) 576-8401  
Fax: (865) 576-5728  
Email: **[reports@osti.gov](mailto:reports@osti.gov)**

### **Disclaimer**

This report was prepared as an account of work sponsored by an agency of the United States Government. Neither the United States Government nor any agency thereof, nor UChicago Argonne, LLC, nor any of their employees or officers, makes any warranty, express or implied, or assumes any legal liability or responsibility for the accuracy, completeness, or usefulness of any information, apparatus, product, or process disclosed, or represents that its use would not infringe privately owned rights. Reference herein to any specific commercial product, process, or service by trade name, trademark, manufacturer, or otherwise, does not necessarily constitute or imply its endorsement, recommendation, or favoring by the United States Government or any agency thereof. The views and opinions of document authors expressed herein do not necessarily state or reflect those of the United States Government or any agency thereof, Argonne National Laboratory, or UChicago Argonne, LLC.

# **Evaluation of statistical variation of microstructural properties and temperature effects on creep fracture of Grade 91**

---

Applied Materials Division  
Argonne National Laboratory

September 2018

## **Prepared by**

**A. Rovinelli, Argonne National Laboratory**  
**M. C. Messner, Argonne National Laboratory**  
**D. M. Parks, DR&C, Inc.**  
**T.-L. Sham, Argonne National Laboratory**



## **Abstract**

This report describes three improvements made to a physically-based model for creep and creep rupture in Grade 91 steel developed as part of the Advanced Reactor Technologies program:

1. Progress on transitioning the model framework to the MOOSE finite element package to improve parallel scalability, increase the physical size of the simulations, and incorporate multiphysics effects into the model.
2. The development of a physically-based method of scaling the model parameters to accurately capture creep in Grade 91 for temperatures in the range of 450° to 500° C.
3. Extending the model to account for microstructural statistical variations, specifically capturing the effect of grain boundary energy on the physical parameters underling the model for grain boundary void nucleation and cavitation.

Put together, these improvements result in an accurate, predictive model for the physical response of Grade 91 steel over the expected use temperature range for the material in future liquid metal cooled fast reactors. The model can be used to more accurately predict engineering properties of the material for very long service lives, which could lead to safer, more economical future advanced reactors.



## Table of Contents

Abstract	i
Table of Contents	iii
List of Figures	v
List of Tables	ix
1 Introduction	1
1.1 Summary of previous results . . . . .	1
1.2 Extending the existing model . . . . .	3
2 Interface-cohesive modeling in MOOSE	5
2.1 Mesh modifier . . . . .	5
2.2 Interface material model . . . . .	6
2.3 Cohesive interface kernel . . . . .	9
2.4 Results . . . . .	10
2.5 Stress assisted vacancy diffusion . . . . .	15
3 The effect of temperature on the model parameters	21
3.1 Material properties and scaling rules . . . . .	21
3.2 Determining the scaling constants . . . . .	24
3.3 Comparing the temperature-dependent model to experimental data . . . . .	26
4 Incorporating microstructural statistical variation in the model	31
4.1 Correlating the GB energy to five parameters grain boundary space . . . . .	34
4.2 Choosing GB properties a functions of GB energy . . . . .	38
4.3 Assessing the effect of crystallography-depedent grain boundary properties .	42
4.4 Supplementary material: Details on the calculation of the grain boundary character . . . . .	44
4.4.1 Grain Boundary Disorientation . . . . .	44
4.4.2 The tilt and twist angle of a GB . . . . .	53
4.4.3 Grain boundary classification . . . . .	53
5 Conclusions	55
Acknowledgments	57
Bibliography	59
Distribution List	65



## List of Figures

1.1	The representative volume element used for the Grade 91 simulations. The grain boundary cohesive elements are two dimensional and conformal to the grains. Different colors represent different grain orientations. . . . .	2
2.1	Schematic representing the steps required to break a monolithic mesh using blocks (e.g. grains): (a) Identify nodes at the interface between blocks, (b) add nodes according to their multiplicity and assign them to the proper element, (c) assign interfaces (e.g. element faces) between blocks, and (d) use interfaces to add lower-dimensional elements on both side of the interface. Arrows represent the linkage between the surface quadrature points used for calculations across the interface. . . . .	7
2.2	Example of a 2D mesh representing a polycrystalline aggregate divided into blocks: (a) the black line represents the cohesive interface between grains and (b) the cohesive interface in (a) is partitioned by grain pairs to allow for different grain boundary behavior. . . . .	8
2.3	(a) Example of a 3D mesh representing polycrystalline aggregate and (b) the resulting 3D cohesive interface between grains. . . . .	8
2.4	Demonstration of the cohesive interface response for pure normal displacement (z direction). (a) undeformed configuration; (b) 3D view of the mesh (color scale represents the displacement magnitude); (c) cohesive interface response with respect to the applied normal displacement. . . . .	12
2.5	Demonstration of the cohesive interface response for an applied pure shear displacement (y direction). (a) undeformed configuration; (b) 3D view of the mesh (color scale represents the displacement magnitude); (c) cohesive interface response with respect to the applied tangential displacement displacement. . . . .	13
2.6	Demonstration of the cohesive interface response for an applied mixed-mode displacement condition (x,y and z). (a) undeformed configuration; (b) 3D view of the mesh (color scale represents the displacement magnitude) and arrows represent the displacement of the interface; (c) cohesive interface response with respect to the simulated time. The tangential component of the average interface stress are parallel to the x and y axis. . . . .	14
2.7	Demonstration of the cohesive interface response for an applied normal displacement on the top surface of Block 2: (a) undeformed configuration; (b) 3D view at maximum shear load for the side faces of Block 2; (c) response of the cohesive interface on each face of Block 2 with respect to model time. Each line represent a component of the average stress. . . . .	16
2.8	(a)-(c) Distribution of the hydrostatic stress for the three simulations, details in Table 2.4. (d) The volume-average hydrostatic stress with respect to the applied nominal strain. . . . .	19
2.9	(a)-(c) Distribution of the von Mises equivalent stress for the three simulations, details in Table 2.4. (d) The volume average von Mises equivalent stress with respect to the applied nominal strain. . . . .	20

3.1	The points are values of the temperature-dependent $S_y$ for Grade 91 from the ASME Code. The line is a best-fit to the MTS form. . . . .	25
3.2	Best fit of the MTS form to the difference between the ASME Code $S_u$ and $S_y$ . . . . .	25
3.3	Model simulations of creep at 150 MPa and several different temperatures. . . . .	27
3.4	Comparison between the physically-based CPFEM model and experimental results at 600° C. The figure plots the experimental data in black and the model results in red. . . . .	28
3.5	Comparison between the physically-based CPFEM model and experimental results at 500° C. The figure plots the experimental data in black and the model results in red. . . . .	29
3.6	Comparison between the physically-based CPFEM model and experimental results at 550° C. The figure plots the experimental data in black and the model results in red. . . . .	29
3.7	Comparison between the physically-based CPFEM model and experimental results at 650° C. The figure plots the experimental data in black and the model results in red. . . . .	30
4.1	Grain boundary energy for BCC <i>Fe</i> as function of disorientation angle (a) and $\Sigma$ value (b). Highlighted values of GB energy for all the simulated $\Sigma 3$ GBs. Data from [43] . . . . .	33
4.2	(a) Comparison of $\Sigma 3$ GB energy (Ni) and void denuded zone width (Cu) as function of the inclination angle. GB energy (blue points) data from [37] and void-denuded zone (red points) data from Han et al. [16] (b) Comparison of $\Sigma 3$ GB energy (Fe) and void denuded zone width (Cu) as function of the inclination angle. Note that void denuded zone data have been plotted using Eq. 4.3. GB energy data from [43]. . . . .	35
4.3	Interpolation of the energy of $\Sigma 3$ GBs with respect to the inclination angle $\Psi$ using different polynomial orders. . . . .	36
4.4	(a) Area-weighted disorientation distribution of the GBs present in the RVE. The contribution of random and CSL boundaries is also highlighted. (b) Area fraction of CSL GB for each $\Sigma$ . . . . .	37
4.5	Comparison of the distribution of the energy of random GBs against data available from [43] . . . . .	38
4.6	(a) Energy of GBs present in the simulate RVE against disorientation angle; (b) Area-weighted distribution of GB energies normalized against the total GB area) [43] . . . . .	39
4.7	Comparison of the distribution of GB properties obtained for 600° C using the GB energy model and a two order of magnitude property range: (a) GB diffusivity, (b) GB viscosity, (c) Nucleation rate . . . . .	41
4.8	Comparison of the macroscopic cell strain rate decomposed into mechanisms within the grains and along the grain boundaries for the standard and crystallographic dependent GB models. Stress level is 60MPa. . . . .	45
4.9	Comparison of the macroscopic cell strain rate decomposed into mechanisms within the grains and along the grain boundaries for the standard and crystallographic dependent GB models. Stress level is 100 MPa. . . . .	46

4.10	Comparison of the macroscopic cell strain rate decomposed into mechanisms within the grains and along the grain boundaries for the standard and crystallographic dependent GB models. Stress level is 140 MPa. . . . .	47
4.11	Comparison of the macroscopic cell strain rate in the loading direction decomposed into mechanisms within the grains and along the grain boundaries for the standard and crystallographic dependent GB models. Stress level is 60 MPa. . . . .	48
4.12	Comparison of the macroscopic cell strain rate in the loading direction decomposed into mechanisms within the grains and along the grain boundaries for the standard and crystallographic dependent GB models. Stress level is 100 MPa. . . . .	49
4.13	Comparison of the macroscopic cell strain rate in the loading direction decomposed into mechanisms within the grains and along the grain boundaries for the standard and crystallographic dependent GB models. Stress level is 140 MPa. . . . .	50
4.14	Comparison of the normalized cavity radii obtained by the two models for the five strongest GBs present in RVE. Stress level is 60MPa and the time is at the onset of damage in the standard model. . . . .	51
4.15	Comparison of the normalized cavity radii obtained by the two models for the five strongest GBs present in RVE. Stress level is 60MPa and the time is the onset of damage in the vary-properties model. . . . .	51
4.16	Comparison of the normalized cavity radii obtained by the two models for the five strongest GBs present in RVE. Stress level is 60MPa and the time is at simulation breakdown. . . . .	52



## List of Tables

2.1	$3DC$ parameters used in all cohesive modeling simulations . . . . .	11
2.2	bulk material property for cohesive simulations . . . . .	11
2.3	Imposed displacement rates for the mixed mode simulation (Figure 2.6) . . .	11
2.4	Embedded physics in test case simulations. . . . .	18
3.1	Parameters for the grain bulk part of the composite model. . . . .	22
3.2	Parameters for the grain boundary part of the composite model. . . . .	22
3.3	Temperature dependent elastic constants. . . . .	24
3.4	Values of the dislocation creep strengths $\tau_y$ and $\tau_v$ and the initial hardening slope $\theta_0$ . . . . .	26
3.5	Temperature dependent rate sensitivity constants. . . . .	26
3.6	Temperature dependent grain bulk diffusivity, grain boundary diffusivity, and grain boundary sliding viscosity. . . . .	26
4.1	Decisions in the model on how to scale the GB parameters with GB energy ( $E_{GB}$ ). . . . .	40
4.2	Mean value and imposed range of the crystallographic GB properties. . . .	42
4.3	Comparison of simulation time to breakdown between the standard and crys- tallographic dependent GB model for different stress levels at $600^\circ C$ . . . .	43
4.4	Mean value and imposed range of the crystallographic dependent GB proper- ties. . . . .	44



# 1 Introduction

Grade 91 is a ferritic-martensitic alloy steel originally developed for use in the Clinch River Breeder Reactor [47, 51]. The material has good high temperature strength, low thermal expansion, high thermal conductivity, and good sodium compatibility. These properties make it an excellent candidate material for intermediate heat exchangers and steam generators in future sodium fast reactors (SFRs).

To reduce the normalized cost of electricity generation some advanced reactor concepts are considering long, 60-year initial design lives [6]. These long design lives require corresponding long-term design allowable stresses. 60-year experiments are not practical and so these allowable stresses must be based on shorter-term creep rupture testing. The traditional American Society of Mechanical Engineers Boiler and Pressure Vessel Code (ASME BPVC) method of extrapolating from short-term experimental tests to long-life design allowable stresses is empirical and hence subject to error when extrapolating too far from the underlying experimental database. Physically-based models could provide more accurate predictions of long-term allowable stresses in Grade 91 as well as examine other engineering design issues like notch strengthening or weakening effects.

## 1.1 Summary of previous results

This work describes several extensions to a physically-based crystal plasticity finite element method (CPFEM) model for creep rupture in Grade 91 steel developed as part of the Advanced Reactor Technologies program. The baseline model and important simulation results have been described in previous reports issued by Argonne National Laboratory [9, 31]. While the focus of this report is on extensions to this base model, this section outlines the purpose and form of the base model along with some of the key results obtained through simulations of long-term creep rupture.

The model has three components: a single crystal, grain bulk model, a grain boundary (GB) cavitation model, and the CPFEM framework tying the two together in a representative volume element (RVE) of Grade 91 microstructure.

The grain bulk model represents the contributions of dislocation motion and vacancy diffusion towards inelastic deformation. A mechanical threshold stress (MTS) model represents hardening and softening caused by the accumulation and recovery of dislocation structure [25]. A linear viscous term represents vacancy diffusion in the grain bulk, calibrated to the grain bulk diffusivity of Grade 91.

The grain boundary model is the cumulation of several decades of work on the mechanisms of void nucleation and cavitation on grain boundaries [8, 35, 45, 55]. The model represents both dislocation and grain boundary diffusion mediated void cavitation. A simple power law in stress represents void nucleation on the boundaries.

The CPFEM framework ties the two models together. The finite element framework represents the grain bulk with quadratic tetrahedral finite elements and grain boundaries with corresponding quadratic interface-cohesive elements. The solid elements embed the single crystal bulk model to determine the constitutive response of the grains. Likewise, the interface-cohesive elements embed the grain boundary model to represent grain boundary motion and creep damage.

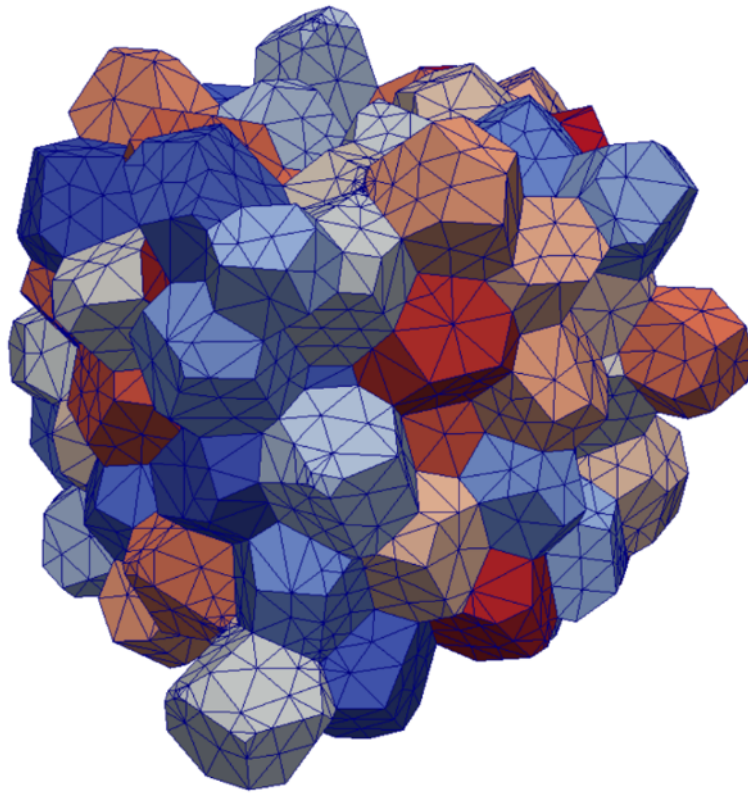


Figure 1.1: The representative volume element used for the Grade 91 simulations. The grain boundary cohesive elements are two dimensional and conformal to the grains. Different colors represent different grain orientations.

Figure 1.1 shows an example of a RVE used to simulate the creep-rupture response of Grade 91. This RVE contains 100 grains and approximately 700 grain boundaries. Periodic boundary conditions are used to impose arbitrary stress and deformation loading on the unit cell. The cell average response represents the macroscale, effective creep characteristics of the material. The microscale response, embedded in the detailed finite element fields, can also be examined to determine microstructural mechanisms for creep and creep-rupture.

For Grade 91, the selected RVE represents only the prior austenite grains (PAGs) and associated GBs. The parameters of the individual grain and GB mechanism models were calibrated to a series of long term creep experiments conducted by Kimura et al. [19] at 600° C. The simulations can then be extended to lower values of applied stress, to represent realistic SFR operating conditions, or to non-uniaxial states of stress to evaluate the effect of stress triaxiality on creep rupture.

The previous reports use this modeling framework to examine several aspects of creep in Grade 91 relevant to engineering design. Key outcomes include finding that grain bulk diffusion tends to become increasingly important at lower stress levels, typical for reactor operating conditions. This change in mechanism from high to low stress causes empirical extrapolation of creep-rupture lives, for example using the Larson-Miller parameter [27], to produce non-conservative design lives. Additionally, while the simulations predict that Grade 91 is notch strengthening at high, experimentally-achievable stresses, the simulations also show that at lower stresses the material becomes notch weakening. Both of these model predictions have implications on the engineering design of structures at elevated temperature, which have been discussed in detail in the previous reports.

## 1.2 Extending the existing model

This report describes extensions to the physically-based model for Grade 91 creep and creep-rupture focusing on three areas.

The previous CPFEM model was implemented in WARP3D ([www.warp3d.net](http://www.warp3d.net)), an open-source finite element package aimed at structural mechanics calculations. Future extensions to the CPFEM modeling framework might incorporate coupled thermo-mechanical simulations of realistic plant transients or extend the model to coupled diffusion-mechanical multiphysics representations of grain boundary cavitation. WARP3D could accommodate these multiphysics simulations without extensive modification. Additionally, parallel scalability on WARP3D is limited to about 1,000 parallel processes, which limits the physical size of the CPFEM calculations. This limitation is not significant for simulations of a periodic RVE representing bulk material behavior but may be limiting for simulations including free surface effects, for example to look at the role of stress concentration in greater detail, or in simulations encompassing a substantial microstructural gradient, for example simulations of a complete weldment including the weld, heat affected zone, and base materials.

The MOOSE finite element framework, developed at Idaho National Laboratory, can simulate multiphysics problems with very good parallel scaling out to 20,000 or more parallel processes [13]. This report describes work in transitioning the CPFEM model framework to MOOSE. The key challenge is the GB model, which requires implementing cohesive-interface models in the framework as MOOSE currently does not have this capability. Once completed, this work will allow us to simulate larger volumes of material and include more detailed,

coupled multiphysics effects in the simulations. Chapter 2 describes progress towards this goal.

All previous reported simulation results are for 600° C, the temperature at which the long-term Kimura creep data is available for calibration. SFR use temperatures for Grade 91 are likely to be lower than this, in the range of 500° to 550° C. This report describes an approach to scaling the model parameters to capture creep in Grade 91 at temperatures from 450° to 650° C. Crucially, this approach does not require recalibrating the model to additional creep data. Rather, the existing parameters, calibrated at 600° C, can be scaled using physically-based scaling relations and available fundamental material constants, for example the activation energy for grain bulk or grain boundary diffusion. Chapter 3 describes the derivation of these physical scaling laws, the identification of the appropriate material properties from literature data, and the results of new simulations at lower and higher temperatures. The chapter validates the new, temperature-dependent model against experimental creep curves. This new model is now available to repeat the studies examining rupture life and notch effects that previous reports carried out at 600° C.

Finally, the base instantiation of the model used constant values of the GB cavitation properties throughout the RVE. However, the GB properties are expected to scale with the crystallography of each individual boundary. Chapter 4 extends the model to capture these crystallographic statistical effects and compares results of these new simulations to the old constant-value results. The overall conclusion is that this refinement is not necessary for capturing macroscopic engineering properties. However, once calibrated this type of model can be used to study the effect of grain boundary engineering on the creep life of the material, to propose modifications to the material processing regimen that could potentially increase the creep-rupture life of the alloy.

## 2 Interface-cohesive modeling in MOOSE

Currently, *MOOSE* does not have an official module to simulate cohesive zone behavior. During the last year, we have extensively collaborated with the *MOOSE* development team to incorporate this capability. This chapter presents the work that has been done to enable cohesive zone modeling (CZM) in *MOOSE*.

Since *Libmesh* [20] itself, which is the finite element library from which *MOOSE* inherits most of its meshing capabilities, does not even contemplate classic cohesive elements, the introduction of CZM in *MOOSE* is not as trivial as it might appear. We elect to extend some of the capabilities already available in *MOOSE* and *Libmesh* to implement CZM, because implementing a new class of elements in *Libmesh* would have significant development overhead. Cohesive zone modeling has been achieved through the introduction of three major component:

1. a mesh modifier,
2. a new interface material model,
3. a cohesive zone interface kernel.

The following sections describe the implementation of each component.

### 2.1 Mesh modifier

Our ultimate goal is to model the behavior of grain boundaries (GBs) opening and sliding therefore a cohesive interface must be defined between each grain. *MOOSE* can modify a mesh prior to and during execution. Because *MOOSE* cannot use a classic cohesive element (e.g. a zero thickness element with integration points defined on the mid plane) the strategy adopted here is to break a monolithic polycrystalline mesh by grains and add the required quadrature points on the grain surface. However, *MOOSE* still need to know the original element neighbors to perform calculations across the interface (e.g. the element connectivity should not be affected by the fact that the mesh has been broken). There are two possible routes to achieve this:

1. use a preprocessor to break the mesh and reconstruct the element connectivity in *MOOSE*
2. load a monolithic mesh and break it directly in *MOOSE*.

Each option has advantages and disadvantages. Option #1 is more efficient because it allows breaking the mesh and generating a GB property input file all at the same time. On the other hand, reconstructing the element connectivity from a broken mesh is much more difficult than splitting it, especially if a distributed mesh is used. Furthermore, *MOOSE* reorders elements to optimize the computational load on each parallel process. This means that even if an element connectivity map is created in the preprocessor it might be useless in the end. Option #2 preserves the original mesh connectivity while breaking the mesh but requires an initial scan of the mesh to generate the GB list to assign different properties to each GB. Furthermore, the initial scan is an operation performed only once *MOOSE* and is quick even for large meshes. Considering the above we choose to implement Option #2.

To break the mesh into grains we followed the approach proposed by Nguyen [36]. For this approach the nodes-to-element map needs to be identified. This is done by looping over all the nodes and finding all the elements sharing each node. Then, we need to loop over all the elements shared by each node, identify which grain each element belongs to, and keep track of the total number of grains connected to the node. The total number of connected grains is the node multiplicity,  $m$ . Node with a multiplicity greater than 1 are classified as interfacial nodes (see Fig. 2.1(a)).  $m - 1$  is the number of times a given node needs to be duplicated to break the mesh (2.1(b)). The original interfacial node is left connected to the element belonging to the grain with the lowest ID number. Added, duplicated nodes are assigned to each of the remaining connected grains and assigned to the proper elements (Fig. 2.1(b)).

To generate a cohesive interface one also needs to identify the adjoining faces of the elements connected to an interfacial node. A shared face between interfacial elements has each of its node as either an interfacial node or one of the duplicated nodes. Therefore, when the splitting is completed one need to loop over each interfacial element and find all its faces embedding only interfacial or duplicated nodes. When such an element face is found we also retrieve the neighboring element and its shared face. Of the two faces, the one with the element belonging to the grain with the lowest ID is added to the list of faces generating the cohesive zone (see Fig. 2.1(c)). The face generating the cohesive interface are then added to a sideset (a group of faces) labeled the master surface (orange region in Fig. 2.1(c)). The opposite side of the cohesive interface is labeled the slave surface. Because we want to be able to assign at each GB a different property, we also keep track of the grain pairs that generate a shared face. This allows the generation of a cohesive interface for each grain pair. When adding interfaces and operating over them with an interface kernel *MOOSE* automatically generates additional surface quadrature points on the elements on both side of the interface. These quadrature points will be used to collect information to model the cohesive zone behavior (Fig. 2.1(d)).

The *C++* code performing these actions, together with a set of tests for the reliability of the mesh modifier, have been merged into *MOOSE* under the name *BreakMeshByBlock*. Furthermore, the Python code used by to generate the mesh input file for *WARP3D* has been upgraded to generate meshes compatible with *MOOSE*.

Figure 2.2 is an example of a 2D monolithic polycrystalline mesh broken using the *BreakMeshByBlock* routine. In Fig. 2.2(a) a single cohesive interface is generated, while in Fig. 2.2(b) the cohesive interface has been partitioned by GB pairs. Figure 2.3 is a 3D example of monolithic polycrystalline mesh broken using the *BreakMeshByBlock*.

The only limitation of *BreakMeshByBlock* regards inserting a cohesive interface between grains at the opposite faces of a periodic RVE. We are working with the *MOOSE* development team to understand the best way to implement this feature.

## 2.2 Interface material model

To describe the behavior of a stateful cohesive zone and to probe stateful material properties on both side of the cohesive interface in sync we had to implement an interface material model. *MOOSE* currently has boundary materials but it does not synchronize material properties across the interface. Furthermore, a boundary is different from an interface: the

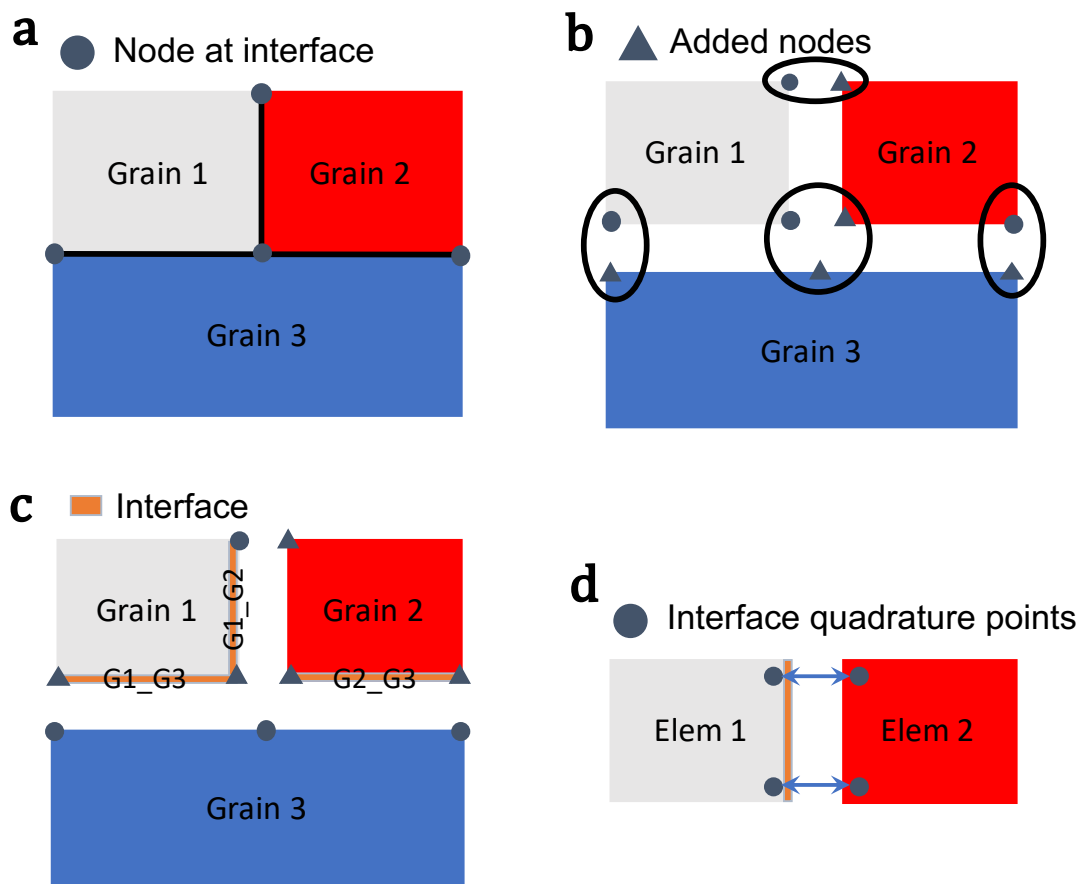


Figure 2.1: Schematic representing the steps required to break a monolithic mesh using blocks (e.g. grains): (a) Identify nodes at the interface between blocks, (b) add nodes according to their multiplicity and assign them to the proper element, (c) assign interfaces (e.g. element faces) between blocks, and (d) use interfaces to add lower-dimensional elements on both side of the interface. Arrows represent the linkage between the surface quadrature points used for calculations across the interface.

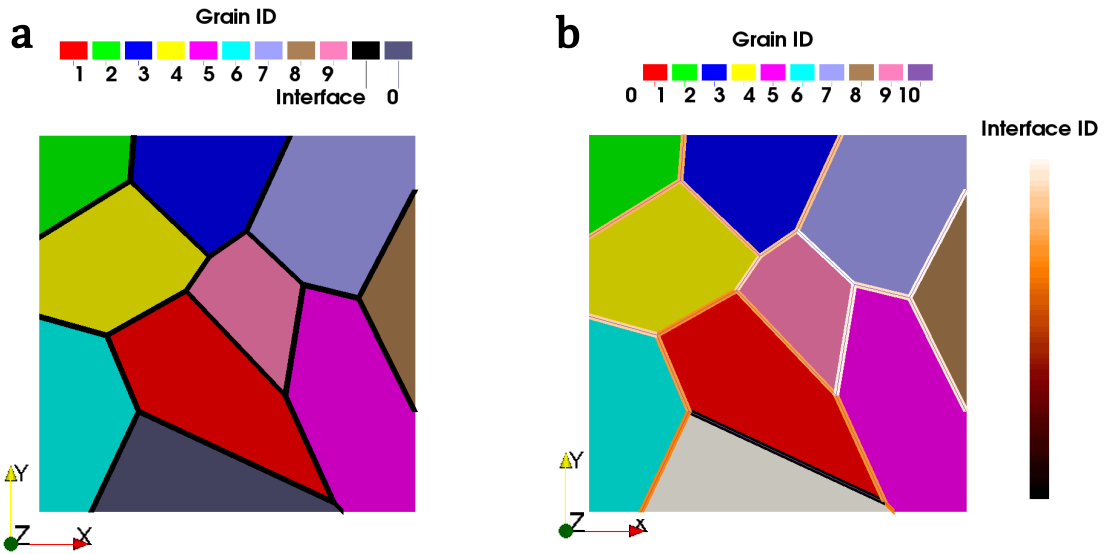


Figure 2.2: Example of a 2D mesh representing a polycrystalline aggregate divided into blocks: (a) the black line represents the cohesive interface between grains and (b) the cohesive interface in (a) is partitioned by grain pairs to allow for different grain boundary behavior.

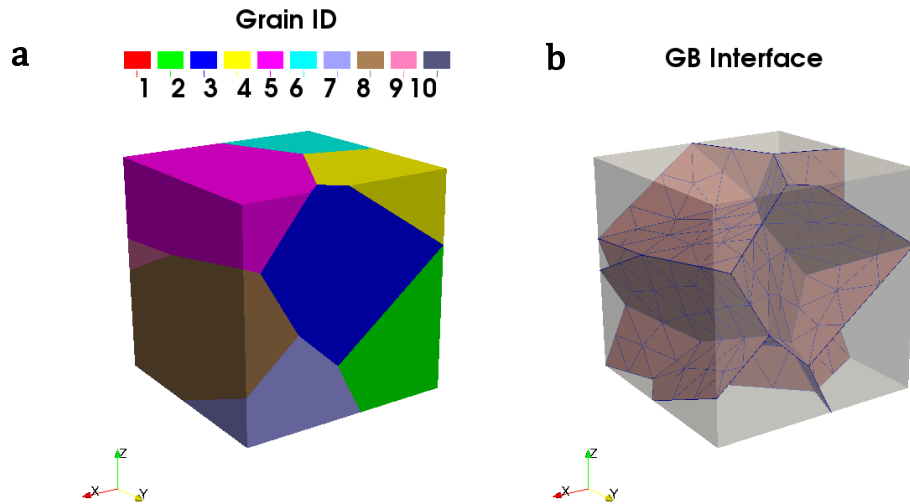


Figure 2.3: (a) Example of a 3D mesh representing polycrystalline aggregate and (b) the resulting 3D cohesive interface between grains.

former is a geometrical entity without mechanics while the latter is also a geometrical entity but it has its own constitutive behavior. A true interface requires integration points to store the interface stateful variables.

The new material model encompasses two *MOOSE* elements:

- a special boundary material (e.g. cohesive interface material),
- an interface user object synchronizing bulk material properties on either side of the interface.

The interface material is a modification of a *MOOSE* boundary material. To make the implementation of different cohesive laws easier we created a specialized cohesive interface material class named *CohesiveMaterialBase*. This class provides the common routines utilized for most or all CZMs, such as rotating from the global reference system to the natural element reference system. Classes inheriting from *CohesiveMaterialBase* to implement a cohesive model must compute the tractions and their partial derivatives with respect to the displacement components. This information must be computed at each quadrature point on the master side of the interface and stored as material properties. A cohesive material is also responsible for updating stateful interface properties. The cohesive interface kernel will then use this information to minimize the residual of the displacement jump while enforcing traction continuity on both side of the interface. To allow the *CohesiveMaterialBase* and all its children to use the updated variable values and bulk material properties, it was necessary to implement the *interfaceUserObject*. The *interfaceUserObject* is a specialized user object that probes variables and material properties on either side of the cohesive interface after they have been updated. Specifically, before each linear iteration the interface user object triggers the evaluation of bulk material properties on both side of the interface and stores the updated properties. After the update of bulk material property, the *interfaceUserObject* collects the relevant quantities at each quadrature point and store them for future use by the interface material. New cohesive laws are implementing by specializing the interface material and interface user objects.

## 2.3 Cohesive interface kernel

The interface kernel available in *MOOSE* enforces a relationship between the values of two variables on the boundary between domains. The interface kernel is based on a discontinuous Galerkin approach and can impose conditions on both fluxes and variables across an interface. However it is not designed to update and store stateful interface parameters, requiring a new object called a *interfaceMaterial*.

A traction separation law is defined by a constitutive model linking the traction ( $\mathbf{t}$ ) on both side of an interface to the displacement jump  $\Delta \mathbf{u}$  (e.g. Eq. 2.1). In what follow the displacement jump will be defined as

$$\mathbf{t} = f(\Delta \mathbf{u}) \quad (2.1)$$

$$\Delta \mathbf{u} = \mathbf{u}^S - \mathbf{u}^M \quad (2.2)$$

where the superscripts  $S$  and  $M$  identify the slave and master surface of the cohesive interface, respectively.

In general, finite elements works by minimizing the energy, defined as the inner product between a variable field and a corresponding complementary generalized force. The *MOOSE* tensor mechanics module solves for the displacements fields, thus nodal forces are the natural component. Therefore, given the traction continuity required by the global equilibrium condition we use the interface kernel to impose the following residual on each component (denoted by the index  $i$ ) of the displacement field:

$$\begin{aligned} R_i^M &= (t_i^M - t_i^S) \Psi^M \\ R_i^S &= (t_i^S - t_i^M) \Psi^S \end{aligned} \quad (2.3)$$

where  $\Psi^M$  and  $\Psi^S$  are the test functions of the master and slave surfaces, respectively. When using a discrete Galerkin approach we need to impose the residual on both side of the interface with the correct sign. By imposing an equal and opposite residual we are enforcing traction continuity, by minimizing the residual the interface kernel weakly imposes stress equilibrium.

The *MOOSE* interface kernel can impose a residual only on a pair of scalar variables (one on each side of the interface). Thus, to completely describe a 3D cohesive law, one need to use three interface kernels, one for each component of the displacement field. Furthermore, cohesive interface laws typically work on the element natural coordinate system (e.g. the normal component of the displacement jump is always perpendicular to the element face and the tangential components are always embedded in the plane of the element face). However, *MOOSE* requires the residual in global reference system. Rotation operators are required to make these changes of coordinates. These rotation procedures are standardized and have been implemented into the *cohesiveMaterialBase* class created to handle CZM.

## 2.4 Results

A few test case simulations have been used to validate our implementation. The non-stateful traction separation law used for testing the model is the phenomenological, 3D coupled, mixed mode cohesive zone model called *3DC* proposed by Salehani and Irani [44] and described by the following equation:

$$t_i = \frac{\sigma_i \lambda_i \Delta u_i}{\delta_i} \exp \left[ - \sum_{j=1}^3 \left( \frac{\Delta u_j}{\delta_j} \right)^\alpha \right] \quad (2.4)$$

where the indexes  $i$  and  $j$  identify the opening ( $i, j = 1$ ) and sliding modes ( $i, j = 2, 3$ ),  $\sigma_i$  is the maximum allowable stress,  $\delta u_i$  is a reference displacement jump and  $\alpha$  and  $\lambda$  are model parameters defined below.

$$\alpha = \begin{cases} 1 & i, j = 1 \\ 2 & i, j \neq 1 \end{cases} \quad \lambda = \begin{cases} e & i, j = 1 \\ \sqrt{2}e & i, j \neq 1 \end{cases} \quad (2.5)$$

	$i$	$\sigma_i [MPa]$	$\delta_i [mm]$	$\Delta u_i^{\sigma_{MAX}} [mm]$
Normal	1	100	1	1
Tangential	2,3	70	0.5	$\approx 0.35$

Table 2.1:  $3DC$  parameters used in all cohesive modeling simulations

$E [GPa]$	$\nu$
50e7	0.3

Table 2.2: bulk material property for cohesive simulations

The value of  $\Delta u_i$  at which maximum stress will occur is

$$\Delta u_i^{\sigma_{MAX}} = \frac{\delta_i}{\sqrt{\alpha_i}} \quad (2.6)$$

This model has been selected as a candidate for development because it has a continuous cohesive behavior with respect to the displacement components, thus allowing us to work on implementing the required *MOOSE* features without worrying about convergence problems caused by discontinuities in the cohesive law. The cohesive parameters and bulk material parameters used in the simulations are listed in Table 2.1 and 2.2, respectively. Results are presented in terms of interfacial stress components and not the tractions, because the stresses are easier to compare with the  $3DC$  model parameters which are defined in terms of stress.

Figures 2.4 and 2.5 depict results for simple opening and simple shear. Opening and shear are applied by imposing a monotonically increasing displacement on the top block. As expected, the maximum stress is obtained at theoretical values of 1 and  $\approx 0.35 [mm]$  for the pure opening and pure sliding condition, respectively (compare with Table 2.1).

Figure 2.6 shows CZM results for mixed mode conditions. In this case a complex displacement has been imposed to the top surface (see Table. 2.3 ). As expected, all the components of the interfacial stress exhibit their peak values at the same point in time (e.g.  $\approx 45 [s]$ ). This behavior is expected because the  $3DC$  model assumes that all the component of the displacement jump contribute to the interface response. Furthermore, the value of each component of interfacial stress are proportional to the displacement jump imposed in each direction (e.g. the higher jump in the normal direction imposes a higher interfacial stress in that direction).

To further validate the CZM implementation, we also considered a simulation with a more complex geometry. In this simulation the top block is further partitioned to include a multi point junction on the interface. There are three interface: (i) one between Blocks 0 and 1, (ii) one between Blocks 0 and 2 and (iii) one between Blocks 1 and 2 (see Fig. 2.7).

Displacement rate $[mm/s]$		
X	Y	Z
0.0025	0.005	0.01

Table 2.3: Imposed displacement rates for the mixed mode simulation (Figure 2.6)

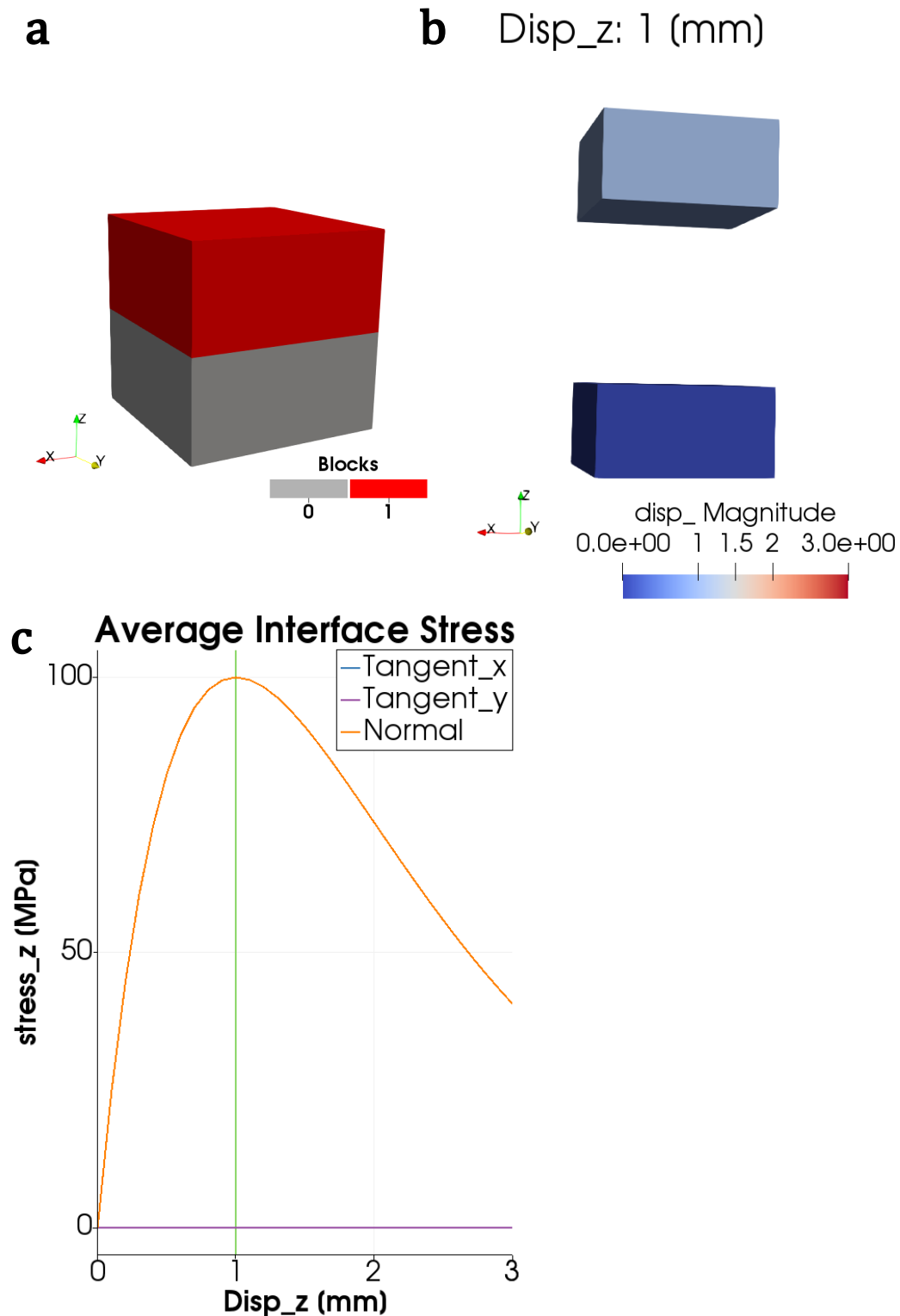


Figure 2.4: Demonstration of the cohesive interface response for pure normal displacement (z direction). (a) undeformed configuration; (b) 3D view of the mesh (color scale represents the displacement magnitude); (c) cohesive interface response with respect to the applied normal displacement.

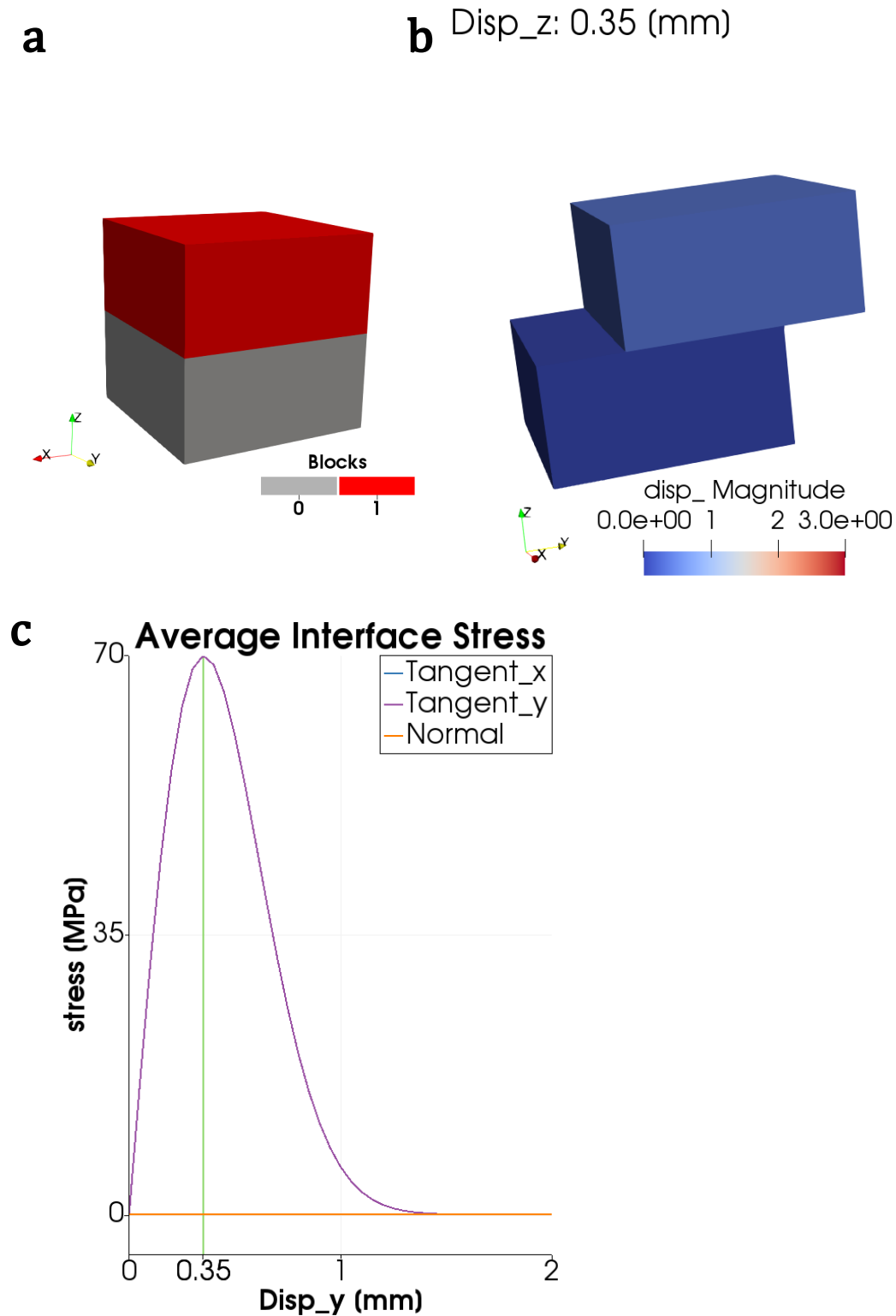


Figure 2.5: Demonstration of the cohesive interface response for an applied pure shear displacement (y direction). (a) undeformed configuration; (b) 3D view of the mesh (color scale represents the displacement magnitude); (c) cohesive interface response with respect to the applied tangential displacement displacement.

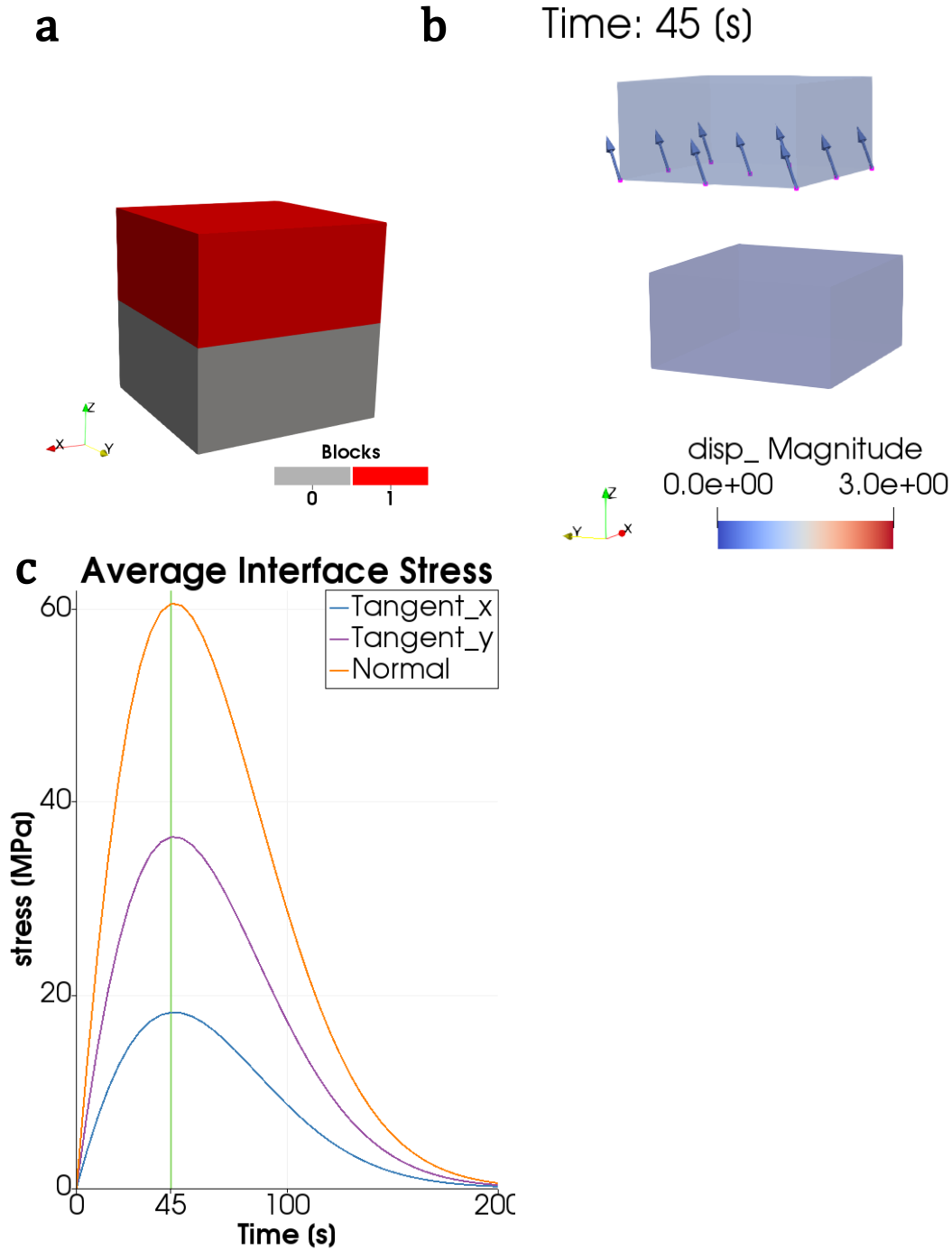


Figure 2.6: Demonstration of the cohesive interface response for an applied mixed-mode displacement condition (x,y and z). (a) undeformed configuration; (b) 3D view of the mesh (color scale represents the displacement magnitude) and arrows represent the displacement of the interface; (c) cohesive interface response with respect to the simulated time. The tangential component of the average interface stress are parallel to the x and y axis.

All the interfaces and blocks have been assigned the same properties. The bottom surface of Block 0 is kept fixed while a constant displacement rate of 0.01 [mm/s] is imposed on the top surface of Block 2 in the Z direction. On the same surface the X and Y and displacement components are fixed to 0. The surfaces of Block 1 do not have boundary conditions applied. The average interface stress of each face of Block 2 is depicted in Fig. 2.7(c) as a function of time and partitioned for each stress component. Face Z of Block 2 is subject only to opening mode, while faces X and Y are subjected to opening plus sliding.

The maximum stress for Face Z happens at a model time of 100 [s] (e.g. imposed displacement jump of 1 [mm]), as expected. Moreover, faces X and Y show the same normal stress values and opposite and equal sliding stresses, which again, are expected because of the symmetry of the problem. For Faces X and Y, the difference in the time of the peak stress for sliding and opening component is a consequence of the complex motion of Block 1 with respect to Block 2. This complex motion is generated by both the imposed boundary conditions and the mechanical response of the interface between Block 0 and Block 1.

The implementation achieves quadratic convergence in all the simulations, using the standard Newton's method as the nonlinear solver. This implies the implemented Jacobian of the equations is consistent.

## 2.5 Stress assisted vacancy diffusion

In a previous report [31] a diffusional strain mechanism was proposed and embedded into *WARP3D* to account for vacancy-induced diffusional creep. In this section we present improved model of grain bulk diffusional creep that leverages MOOSE's multiphysics capabilities.

Assuming that defect diffusion is driven by both concentration and a pressure gradient, the defect flux can be written as

$$\mathbf{J} = -D\nabla c + k_p c \nabla P \quad (2.7)$$

where  $D$  is the diffusion coefficient,  $c$  is the defect concentration,  $P$  is the pressure and  $k_p$  is a convection coefficient. As a first order approximation we will consider  $D$  and  $k_p$  as isotropic material constants. Including mass conservation, the governing equation for the stress assisted diffusion can be written as:

$$\int_V \frac{dc}{dt} dV = \int_V \nabla \cdot (D\nabla c - k_p c \nabla \sigma_H) dV \quad (2.8)$$

where the pressure  $P$  has been written in terms of the hydrostatic stress  $\sigma_H$ . From a mechanical perspective, defects induce a eigenstrain in the material, thus affecting the material response. With an eigenstrain the stress divergence equation becomes:

$$\int_V \nabla \cdot \sigma dV = \int_V \nabla \cdot (\mathbf{C} : (\varepsilon - \alpha (c - c_0) \mathbf{I})) dV = 0 \quad (2.9)$$

where  $\mathbf{C}$  is the elastic stiffness,  $c_0$  is the stress-free defect concentration,  $\alpha$  is the coefficient relating the defect concentration to the volumetric strain and  $\mathbf{I}$  is the second order identity tensor.

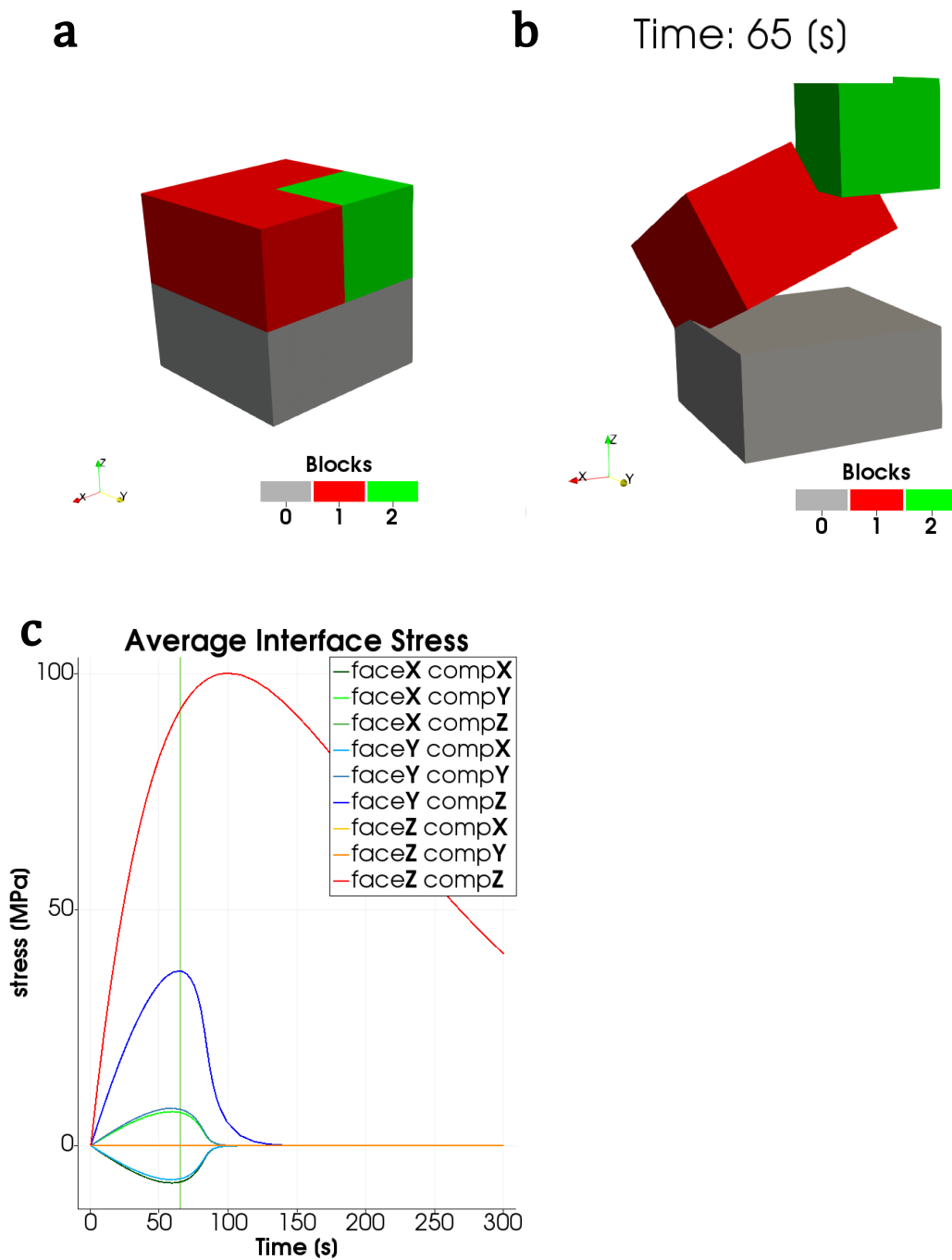


Figure 2.7: Demonstration of the cohesive interface response for an applied normal displacement on the top surface of Block 2: (a) undeformed configuration; (b) 3D view at maximum shear load for the side faces of Block 2; (c) response of the cohesive interface on each face of Block 2 with respect to model time. Each line represent a component of the average stress.

The defect concentration is coupled to the hydrostatic stress and vice versa. Therefore, Eqs. 2.8 and 2.9 need to be solved simultaneously. The *MOOSE* tensor mechanics module already allows for eigenstrains coupled to arbitrary field variables. The complete problem then only requires implementing a kernel for the divergence term. This starts from identifying the residual 2.10 and using the divergence theorem to compute its weak form as

$$R = \int_V \left( \frac{dc}{dt} + \nabla(-D\nabla c + k_p c \nabla \sigma_H) \right) dV \quad (2.10)$$

$$R_{weak} = \int_V \left( \frac{dc}{dt} \Psi + D\nabla c \cdot \nabla \Psi - k_p c \nabla \sigma_H \cdot \nabla \Psi \right) dV \quad (2.11)$$

where  $\Psi$  represents a test function and the surface integral resulting from applying the divergence theorem have been omitted. Equation 2.11 is unstable if the convection term dominates the diffusion term. To prevent oscillations, a streamline upwind, Petrov-Galerkin stabilization scheme is adopted. This stabilization can be implemented by adding a term to the weak form residual:

$$R_{MOOSE} = R_{weak} \cdot (1 + \tau (k_p c \nabla \sigma_H \cdot \nabla \Psi)) \quad (2.12)$$

where  $\tau$  is a function of the mesh size and timestep and defined as

$$\tau = \frac{4}{\Delta t^2} + 4 \left( \frac{\|k_p \nabla \sigma_H\|}{h} \right)^2 + 9 \left( \frac{4D}{h^2} \right)^2 \quad (2.13)$$

where  $\Delta t$  is the simulation time step and  $h$  is the element length.

Three simulations, described here, show the effect of including stress assisted vacancy diffusion. The three simulations consists of an elastoplastic, cylindrical notched specimen subject to axial tension. The first simulation completely neglects the effect of stress-assisted diffusion (i.e.  $D$  and  $k_p$  are set to 0), in the second simulation the diffusion term is included, and in the third simulation the convective term is also included. Table 2.4 summarize the physics embedded in each simulations.

The material parameters used in the simulations are: Young modulus  $E = 21.5 [GPa]$ , Poisson ratio  $\nu = 0.3$ , yield strength  $\sigma_Y = 445 [MPa]$ ,  $\alpha = 0.001 [m^3/mol]$  and  $c_0 = 0 [mol/m^3]$ . The diffusion parameters have been set as  $D = 1 [m^2/h]$ ,  $k_p = 0.1 [m^2/(h MPa)]$ . All the simulations have the same imposed mechanical boundary conditions of a continuously imposed strain rate  $\dot{\epsilon} = 0005 [1/h]$  on the top surface of the cylinder and a fixed bottom surface.

For the simulations including diffusion a concentration flux  $\Phi = 1 [mol/(h m^2)]$  is imposed on the side surface of the cylinder while zero flux is imposed on top and bottom surfaces.

Figures 2.8(a)-(c) compare the hydrostatic stress distribution in the middle of the specimen for the three cases. Figures 2.9(a)-(c) compare the distribution of the von Mises equivalent stress. For both figures, the simulations results are depicted at 3% nominal strain. Both the distribution of the hydrostatic stress and the von Mises stress vary depending on the physics included in the simulations. Subfigures 2.8(d) and 2.9(d) show the volume average hydrostatic and equivalent von Mises stress, respectively, as function of the nominal applied strain. The reference model exhibits the stiffest response, while the models including

Simulation	Included Physics		
	Mechanical	Diffusion	Convection
Reference	Yes	No	No
Only Diffusion	Yes	Yes	No
Diffusion Convection	Yes	Yes	Yes

Table 2.4: Embedded physics in test case simulations.

diffusion are more compliant. This result is expected because injecting defects increases the specimen volume (and therefore its length) without imposing additional stresses. Thus some of the imposed deformation is accommodated by vacancy motion, rather than lattice strain.

This simple example shows that explicitly considering stress-assisted defect diffusion can significantly affect the mechanical response of a system. This simple implementation will serve as a basis to include diffusion assisted creep behavior in both the crystal plasticity and the GB models. The approach proposed here is similar to the one proposed by Pu et al. [40] however, when development will be completed, *MOOSE* will allow to simultaneously solve the mechanical and vacancy diffusion problem on all the domain.

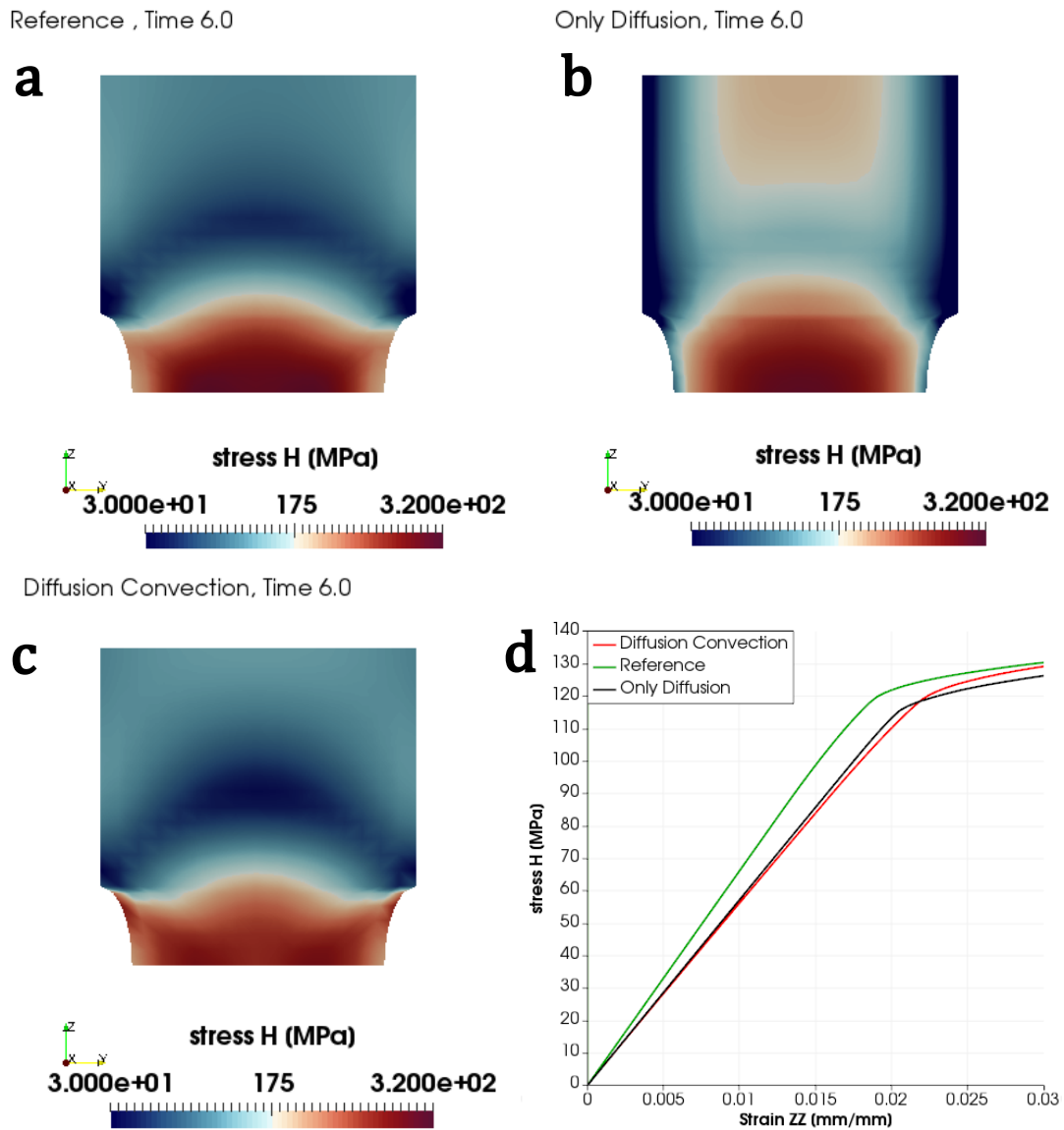


Figure 2.8: (a)-(c) Distribution of the hydrostatic stress for the three simulations, details in Table 2.4. (d) The volume-average hydrostatic stress with respect to the applied nominal strain.

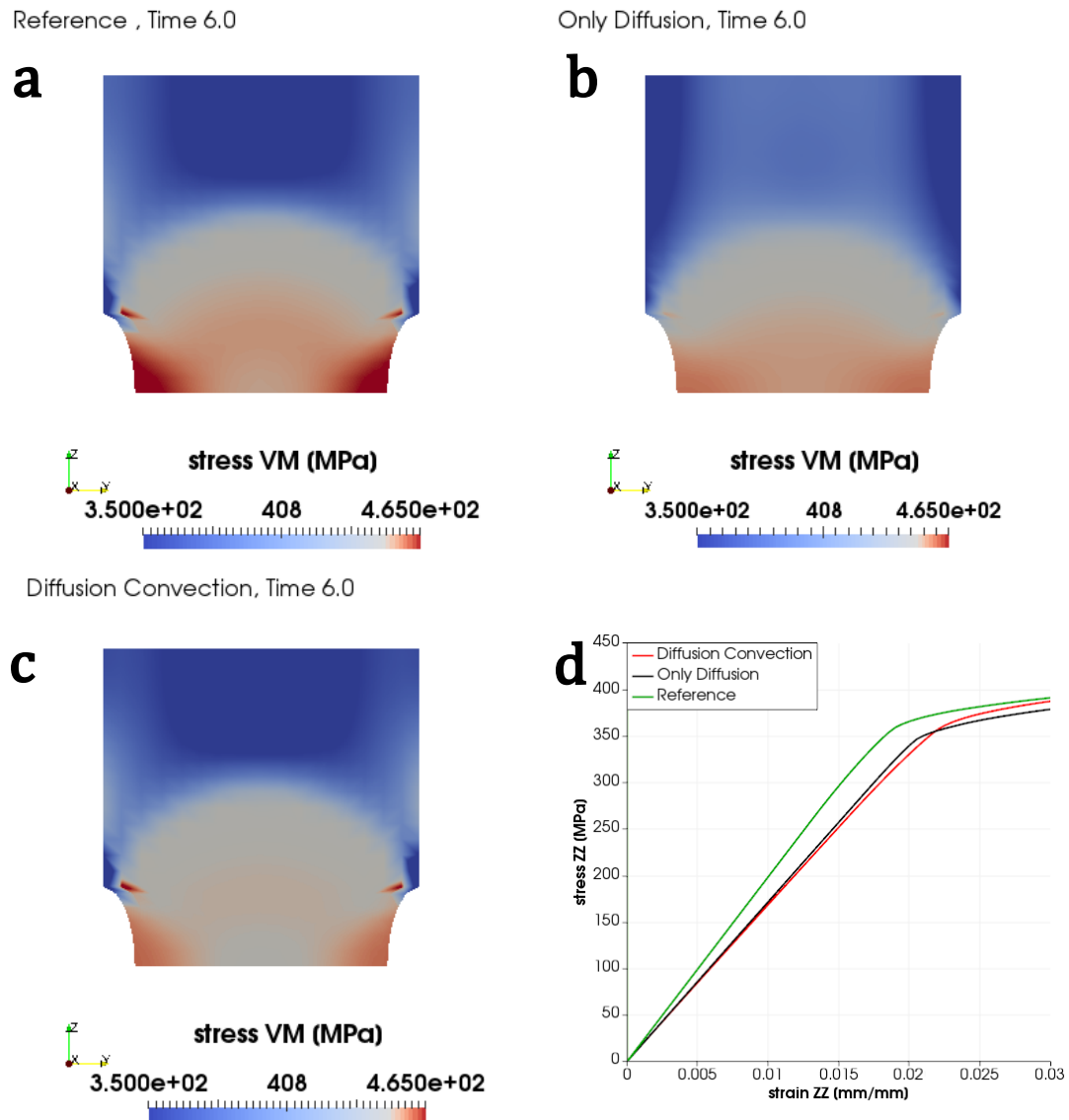


Figure 2.9: (a)-(c) Distribution of the von Mises equivalent stress for the three simulations, details in Table 2.4. (d) The volume average von Mises equivalent stress with respect to the applied nominal strain.

### 3 The effect of temperature on the model parameters

The final microstructural model for creep rupture in Grade 91, described in full in previous reports [9, 31], combines a crystal plasticity model for the grain bulk deformation and a cavitation model coupled to linear viscous grain boundary sliding for the grain boundary deformation. This composite model has successfully reproduced long-term experimental creep test data at 600° C and been used to predict creep-rupture properties and notch effects in Grade 91 material [31].

The model is physically based — the model parameters can be related back to the underlying physical mechanisms of dislocation and diffusion mediated inelastic deformation and void growth. The model parameters are either physical constants or are basic, measurable properties of the material like the bulk diffusivity. The approach to date has required calibration to experimental data to determine parameters related to the strength of internal barriers to dislocation slip, void nucleation, and void growth. Despite requiring calibration the model retains better explanatory and extrapolatory power than an empirical, macroscale creep model. Even though the physical model parameters are calibrated to experiments, they directly represent the underlying physical deformation mechanisms. These mechanisms remain the same under different loading conditions or at different temperatures.

One advantage of a physically-based model is that the material constants should obey some physical temperature scaling law. This means that, ideally, the constants determined for the 600° C should be able to be scaled to higher or lower temperatures without requiring recalibrating the model to new experimental data. This process requires identifying the temperature-dependent material properties, determining the appropriate scaling rule, and determining the physical constants governing that scaling relation. This chapter follows this process for the existing Grade 91 model with the goal of extending the model to cover temperatures in the range of 450° to 650° C, which includes the expected operating conditions for SFR designs.

#### 3.1 Material properties and scaling rules

Tables 3.1 and 3.2 list the material properties defining the composite model for grain and grain boundary deformation. Included in the table are the values of the parameters used in the previous 600° C study. Additionally, the tables comment on whether the parameters are temperature dependent or not and provide a suggested, physical scaling relation.

*Empirical* scaling, used only for the elastic constants, is a best-fit polynomial to tabulated values. While there are several physically-motivated models for elastic properties [34, 48] these values are also widely tabulated from exact experimental measurements. They can be taken as a well-studied constant relating to the atomic lattice. The composite model approximates the single crystal elastic response as isotropic and so the shear modulus, used in several of the temperature scaling relations below, is defined by the temperature-dependent Young's modulus and Poisson's ratio.

*MTS* scaling is based on the concepts of the Mechanical Threshold Stress model for the macroscale material flow stress [10, 22], extended to microscale crystal modeling by Kok et al. [25]. Kok et al. [25] demonstrate that the MTS model has a strong connection to the physics of thermally-activated dislocation recovery. At fixed strain rate, the form of the

Property	Symbol	Value at 600° C	Units	Thermal?	Scaling
Young's Modulus	$E$	150000	MPa	Yes	Empirical
Poisson's ratio	$\nu$	0.285	-	Yes	Empirical
Initial obstacle strength	$\tau_y$	40	MPa	Yes	MTS
Saturated obstacle strength	$\tau_v$	12	MPa	Yes	MTS
Rate sensitivity	$n$	12	-	Yes	Kocks-Mecking
Initial hardening slope	$\theta_0$	800.0	MPa	Yes	Shear modulus
Voce exponent	$m$	1	-	No	-
Bulk diffusivity	$D_G$	$1.2 \times 10^{-9}$	$\text{MPa}^{-1} \cdot \text{hr}^{-1}$	Yes	Arrhenius
Reference strain rate	$\bar{\gamma}_0$	$9.55 \times 10^{-8}$	$\text{hr}^{-1}$	Yes	Kocks-Mecking

Table 3.1: Parameters for the grain bulk part of the composite model.

Property	Symbol	Value at 600° C	Units	Thermal?	Scaling
GB viscosity	$\eta$	$1.0 \times 10^6$	$\text{MPa} \cdot \text{hr} \cdot \text{mm}^{-1}$	Yes	Arrhenius
Initial cavity radius	$a_0$	$5.0 \times 10^{-5}$	mm	No	-
Initial cavity spacing	$b_0$	0.06	mm	No	-
GB diffusivity	$D_{GB}$	$1.0 \times 10^{-15}$	$\text{MPa}^{-1} \cdot \text{hr}^{-1} \cdot \text{mm}^3$	Yes	Arrhenius
Cavity half-angle	$\psi$	75	degrees	No	-
Nucleation stress	$\Sigma_0$	200	MPa	Unknown	-
Nucleation rate	$F_N/N_I$	$2 \times 10^4$	-	Unknown	-
Nucleation exponent	$\beta$	2	-	Unknown	-

Table 3.2: Parameters for the grain boundary part of the composite model.

microstructural MTS model is

$$\tau = \hat{\tau} \left\{ 1 - \left[ \frac{kT}{\mu b^3 g_0} \right]^{1/q} \right\}^{1/p} \quad (3.1)$$

where  $\hat{\tau}$  is the mechanical threshold stress — the slip resistance at absolute zero temperature,  $k$  is the Boltzmann constant,  $T$  is absolute temperature,  $\mu$  is the temperature-dependent shear modulus,  $g_0$  is some normalized thermal activation energy,  $b$  a characteristic Burgers vector, and  $q$  and  $p$  describe the shape of the microscale energy barrier. A *shear modulus* scaling indicates the property scales linearly with the shear modulus. This is the case for the initial hardening slope in both the classical and microstructural MTS models [22].

*Kocks-Mecking* scaling denotes a temperature scaling law derived from the work of Kocks and Mecking [22, 23, 30]. Applied to the classical power law viscoplastic model [31], the Kocks-Mecking scaling predicts the rate sensitivity exponent scales as

$$n = -\frac{\mu b^3}{AkT} \quad (3.2)$$

where  $A$  is some constant and the remaining parameters are defined previously. The theory predicts the reference strain rate will have some moderate temperature dependence, varying inversely with the shear modulus.

Both the grain bulk and grain boundary diffusivity should scale with a classical Arrhenius form

$$D = D_0 e^{-\frac{Q}{RT}} \quad (3.3)$$

where  $D_0$  is a constant (the diffusivity at absolute zero temperature),  $Q$  is an activation energy and  $R$  is the gas constant. These constants have been determined for various alloys and pure materials [12].

Early work by Gifkins and Snowden [14] implies a grain boundary viscosity scaling relation of

$$\eta = \frac{AkT}{D_{GB}} \quad (3.4)$$

where  $A$  is the proportionality constant. Raj and Ashby [41] confirms this general scaling relation and provides a theoretical expression for the prefactor. Langdon [26] derives a similar scaling relation but argues that the stress exponent should be 2, rather the 1 for linear viscous behavior. Later work by Koike et al. [24] has a similar functional relation, but replaces the explicit dependence on the grain boundary diffusivity with a general, thermally-activated scaling relation

$$\eta = \frac{AkT}{\mu \exp\left(-\frac{Q}{RT}\right)}. \quad (3.5)$$

Additionally, these authors allow a general power law dependence on stress. For this work we adopt the simpler form, Eq. 3.4, as the temperature dependence of the grain boundary viscosity is fully defined once the scaling for the grain boundary diffusivity has been determined.

The microstructural parameters describing the initial grain boundary cavity distribution are temperature independent, as they are the result of prior processing before the start of a

Parameter	25° C	450° C	500° C	550° C	600° C	650° C
$E$ (MPa)	213000	182000	179000	175000	165000	155000
$\nu$ (-)	0.29	0.302	0.305	0.308	0.309	0.312
$\mu$ (MPa)	82600	69900	68600	66900	63000	59000

Table 3.3: Temperature dependent elastic constants.

test or service loading. The temperature dependence of the Voce exponent is unknown but likely to be relatively small.

This leaves only the nucleation parameters for the grain boundary cavitation model. There is little to no information available in the literature on the temperature dependence of void nucleation via non-radiation induced mechanisms. As a first approximation the current model keeps this parameters fixed to the values calibrated at 600° C.

### 3.2 Determining the scaling constants

The previous section describes the form of the material property scaling relations for the temperature-dependent model properties. This section determines the scaling parameters from available literature data. The approach adopted here is to use the literature data to set the temperature scaling constants, but then uniformly scale the final model so that all the temperature-dependent constants, with the exception of the elastic constants, pass through the previously-calibrated values at 600° C.

The temperature-dependent Young’s modulus of Grade 91 steel was measured in Takahashi [52]. Takahashi provides values at 550°, 600°, and 650° C. These values were supplemented with the Grade 91 standard value of 213 GPa at room temperature and interpolated linearly between points to generate the values listed in Table 3.3.

Hirose et al. [17] provides temperature-dependent values of Poisson’s ratio for a ferritic-martensitic steel very similar to Grade 91. These values were used to produce the properties in Table 3.3.

Assuming elastic isotropy, as with the previous model for Grade 91, the Young’s modulus and Poisson’s ratio can be used to compute the temperature-dependent shear modulus. Table 3.3 lists these values along with the rest of the elastic constants. Note the properties in Table 3.3 do not match the values used in the previous simulations at 600° C. Rather than scaling the values to match we used the new 600° C values of the elastic constants for the simulations in this chapter.

$\tau_y$  is the initial obstacle density strength opposing dislocation motion. This parameter is tied to the material yield stress. Figure 3.1 plots the temperature-dependent yield stress of Grade 91 as tabulated in Section III, Division 5 of the ASME Boiler and Pressure Vessel Code [3]. The Code values of  $S_y$  lower bound the measured temperature-dependent yield stress of the actual material. However, this scaling will be lost when the data is rescaled to match the microscale parameter at 600° C — the Code data here just gives the temperature dependence of the initial obstacle strength and not the actual values. The line overlaying the points representing the Code data is a best-fit to the MTS model described by Eq 3.1. This best-fit line, scaled to match the calibrated 600° C values of  $\tau_y$ , provides the temperature-

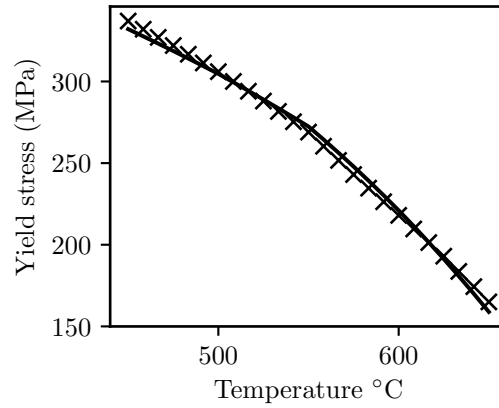


Figure 3.1: The points are values of the temperature-dependent  $S_y$  for Grade 91 from the ASME Code. The line is a best-fit to the MTS form.

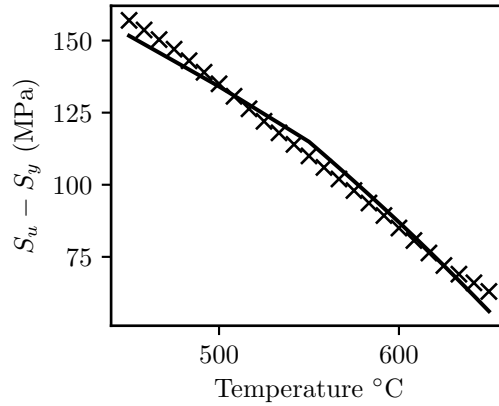


Figure 3.2: Best fit of the MTS form to the difference between the ASME Code  $S_u$  and  $S_y$ .

dependent values listed in Table 3.4.

The ASME Code also provides temperature-dependent values of the ultimate tensile strength,  $S_u$ . The temperature dependence of the microstructural parameter  $\tau_v$  is proportional to the amount of work hardening in the material, roughly  $S_u - S_y$ . Figure 3.2 shows a plot of this difference and a best-fit line to the MTS form. As with  $\tau_y$ , this fit, rescaled to match the calibrated parameter at 600° C, provides the values of  $\tau_v$  shown in Table 3.4.

The initial hardening slope,  $\theta_0$  scales with the shear modulus. Table 3.4 provides values of this parameter using the temperature-dependent shear modulus defined above.

The value of the scaling constant  $A$  in Eq 3.2 can be determined from the previously calibrated value of the rate sensitivity exponent  $n$  at 600° C, the temperature-dependent shear modulus, and the Burgers vector length for  $\alpha$ -Fe of  $b = 2.74 \text{ \AA}$ , Table 3.5 shows the resulting temperature-dependent values of the rate-sensitivity exponent and the reference strain rate. As described above, the reference rate scales inversely with the shear modulus.

Determining the temperature dependence of the grain bulk and grain boundary diffu-

Parameter	450° C	500° C	550° C	600° C	650° C
$\tau_y$ (MPa)	60.1	55.1	49.3	40.0	28.8
$\tau_v$ (MPa)	20.9	18.5	15.8	12.0	7.74
$\theta_0$ (MPa)	888	871	850	800	749

Table 3.4: Values of the dislocation creep strengths  $\tau_y$  and  $\tau_v$  and the initial hardening slope  $\theta_0$ .

Parameter	450° C	500° C	550° C	600° C	650° C
$n$ (-)	16.1	14.8	13.5	12.0	10.6
$\bar{\gamma}_0$ (hr <sup>-1</sup> )	$8.61 \times 10^{-8}$	$8.77 \times 10^{-8}$	$9.00 \times 10^{-8}$	$9.55 \times 10^{-8}$	$1.02 \times 10^{-7}$

Table 3.5: Temperature dependent rate sensitivity constants.

sivities requires identifying an activation energy associated with the appropriate diffusion mechanism. Frost and Ashby [12] provides values of these activation energies, for both grain boundary and bulk diffusion, for a Cr-Mo-V steel. While this material does not exactly match Grade 91's chemical composition, it should be sufficiently similar to determine the temperature dependence of these model parameters by scaling to match the calibrated values at 600° C. The Frost and Ashby values for the two mechanisms are:

$$Q_G = 239 \text{ kJ/mol} \quad (3.6)$$

$$Q_{GB} = 174 \text{ kJ/mol.} \quad (3.7)$$

Based on these values Table 3.6 lists the temperature-dependent diffusivity for both grain bulk and grain boundary diffusion. Equation 3.4 can then be used to compute the values of the sliding viscosity, which are also listed in Table 3.6.

Figures 3.3 shows calculated creep curves using the scaled model parameters at a constant load of 150 MPa and from temperatures from 450° to 650° C. The scaled parameters reasonably describe the effect of temperature on the creep rate and rupture life. Increasing the temperature increases the creep rate and decreases the time to tertiary creep.

### 3.3 Comparing the temperature-dependent model to experimental data

To test the temperature-dependent creep curves predicted by the model this section compares simulated creep tests to available experimental data. The experimental data used in these comparisons was extracted from references [7, 19, 29, 49, 50, 60].

Parameter	450° C	500° C	550° C	600° C	650° C
$D_G$ (MPa <sup>-1</sup> hr <sup>-1</sup> )	$1.30 \times 10^{-12}$	$1.69 \times 10^{-11}$	$1.62 \times 10^{-10}$	$1.20 \times 10^{-9}$	$7.12 \times 10^{-9}$
$D_{GB}$ (MPa <sup>-1</sup> · hr <sup>-1</sup> · mm <sup>3</sup> )	$6.93 \times 10^{-18}$	$4.50 \times 10^{-17}$	$2.33 \times 10^{-16}$	$1.00 \times 10^{-15}$	$3.66 \times 10^{-15}$
$\eta$ (MPa · hr · mm <sup>-1</sup> )	$1.19 \times 10^8$	$1.97 \times 10^7$	$4.04 \times 10^6$	$1.00 \times 10^6$	$2.89 \times 10^5$

Table 3.6: Temperature dependent grain bulk diffusivity, grain boundary diffusivity, and grain boundary sliding viscosity.

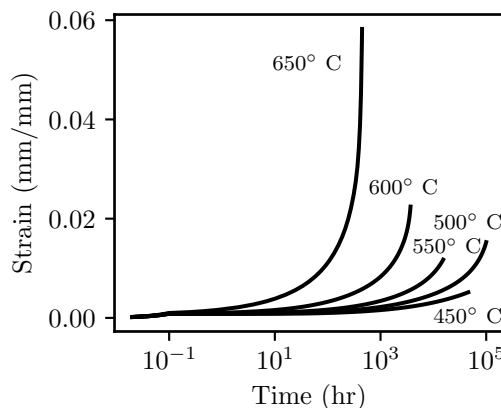


Figure 3.3: Model simulations of creep at 150 MPa and several different temperatures.

Figures 3.4 first shows a comparison between the model and the available experimental data at 600° C. Recall this temperature was where the original model was calibrated to the Kimura data. This plot then is nearly a duplicate of the previous results except:

1. The elastic constants have been altered slightly, as described above.
2. This plots show a comparison to additional experimental data obtained by other researchers using different batches of Grade 91 material.

The change in the elastic constants does not significantly change the simulated creep curves. Though not specifically labeled, it is obvious from the plots which of the experimental data comes from Kimura's work, as the model and experimental curves closely agree. However, the other available experimental data at these conditions shows a much softer response — more creep deformation in the same period of time and a shorter rupture life. Kimura's material seems to generally be more creep-resistant than average Grade 91 material at high temperatures, a trend we should expect the physically based model to replicate.

Figures 3.5, 3.6, and 3.7 then plot similar comparisons at 650°, 550°, and 500° C, respectively. There was insufficient creep data to make a comparison at 450° C. These figures use the temperature-dependent parameters described above, based on the physical scaling laws. There is no additional calibration to experimental data. Overall, the simulated creep curves at the new temperatures compare reasonably with the experimental data. The model predicts a stiffer creep response than most of the non-Kimura experiments at 650° C, which accords with Kimura's material being more creep-resistant than the average response of Grade 91 at high temperatures. The model generally matches the experimental average behavior at 500° and 550°.

Overall, the proposed method of scaling calibrated model parameters to different temperatures produces good agreement to the available creep test data. This is significant as the process requires no additional calibration — the comparisons shown in this section are true validation tests of the model predictions. This new temperature-dependent model can now be used to repeat many of the useful predictions described in previous reports at 600°

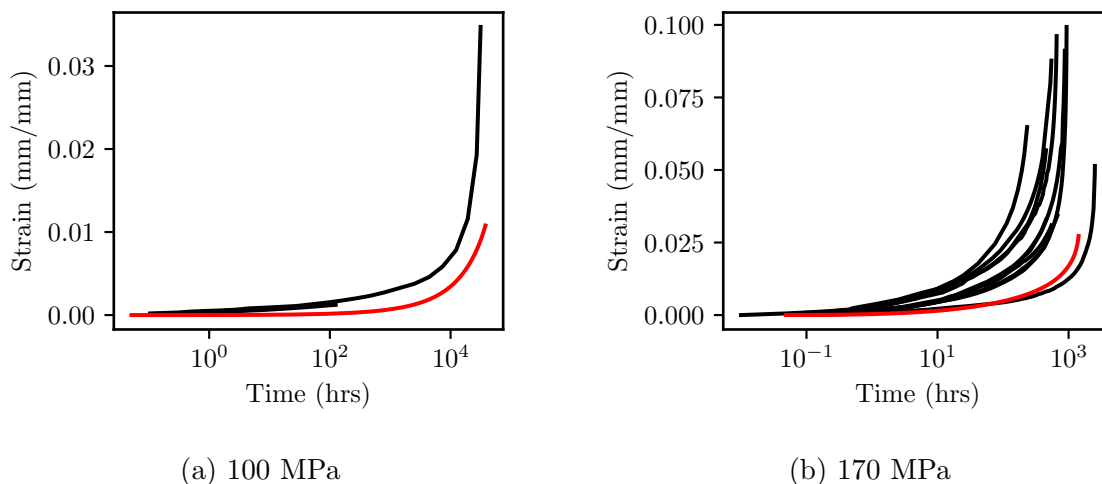


Figure 3.4: Comparison between the physically-based CPFEM model and experimental results at 600° C. The figure plots the experimental data in black and the model results in red.

C. For example, we can use the model to assess notch strengthening or weakening in Grade 91 at lower temperatures more representative of SFR operating conditions.

In engineering use, Grade 91 creeps at temperatures approximately between 450° and 650° C. Below 450° C creep becomes negligible and the alloy has very little creep strength above 650° C. Therefore, this model captures the full creep regime. Based on the accuracy of the model predictions, it is reasonable to assume that the material mechanisms governing creep deformation and represented in the physical model remain the same over these temperatures. For other materials caution would be needed to ensure that new creep mechanisms do not become active as the parameters are scaled farther and farther from the calibration temperature. However, the general approach outlined here could be used to develop temperature dependent CPFEM models for additional materials by calibrating to experimental data at a single temperature and scaling the resulting parameters based on the physical scaling laws described above.

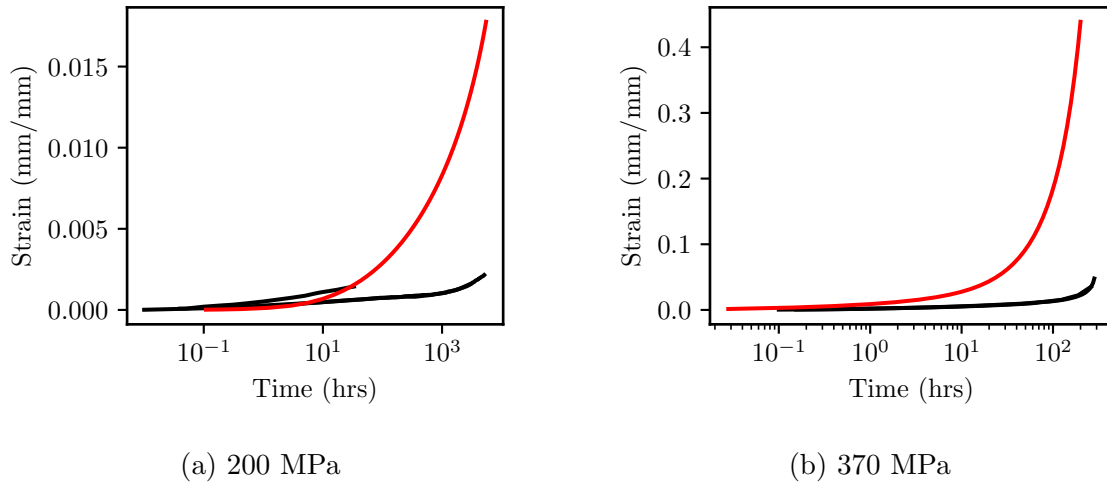


Figure 3.5: Comparison between the physically-based CPFEM model and experimental results at 500° C. The figure plots the experimental data in black and the model results in red.

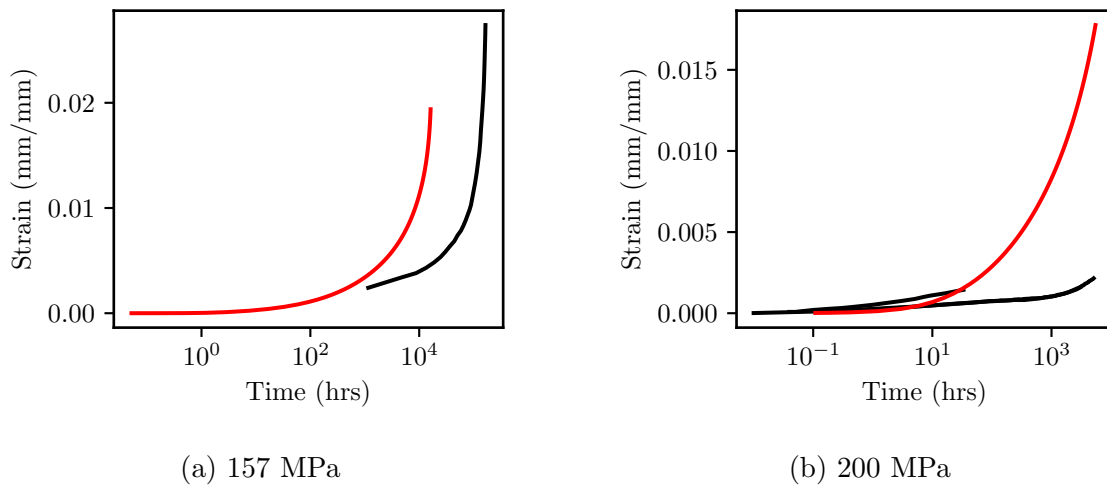


Figure 3.6: Comparison between the physically-based CPFEM model and experimental results at 550° C. The figure plots the experimental data in black and the model results in red.

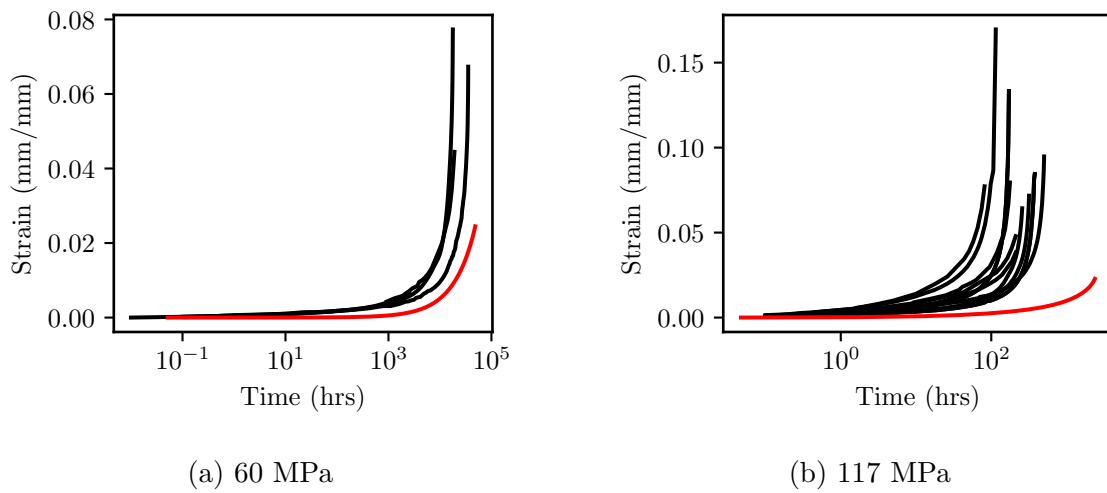


Figure 3.7: Comparison between the physically-based CPFEM model and experimental results at 650° C. The figure plots the experimental data in black and the model results in red.

## 4 Incorporating microstructural statistical variation in the model

Grain boundaries (GBs) are the surface shared by two adjoining crystals. The GB properties are determined by the arrangement of atoms on either side of the GB. This arrangement of atoms generates the so-called GB character which is responsible for the statistical distribution of GB properties in an actual material. The GB character is defined by five macroscopic parameters [15]. Of the five parameters, three are related to the difference in the lattice orientation between the two adjacent crystals (i.e. disorientation) and the other two are related to orientation of the GB plane. Therefore to correctly compute a GB property, such as the GB diffusivity ( $D_{GB}$ ) and sliding viscosity ( $\eta_{GB}$ ), all the five parameters need to be taken into account. However, experimental or atomistic simulation data current does not exist to directly map the five GB parameters onto material properties of interest. A simpler approach would find some intermediate, scalar parameter that directly describes the GB properties of interest.

An early study by Aaron and Bolling [1, 2] advocated the excess free volume as a promising scalar GB parameter. In a recent work, Shvindlerman et al. [46] presented an experimental methodology to measure the excess free volume for all kinds of GBs. However, extensive datasets describing the excess free volume in relations to the five parameter GB space are not available in the literature for body-centered cubic (BCC) crystals such as  $\alpha$ -Fe.

Olmsted et al. [37, 38] computed the properties of 388 GBs via molecular dynamic simulations for two different face-centered cubic (FCC) crystals materials. The pool of simulated GB was constructed to span a vast region of the 5 parameters GB space, focusing on low index GBs (e.g. the [100],[110],[111]) but also including a few high-index axis GBs. A moderate correlation between GB energy and GB excess free volume was found. Wolf [56, 57, 58] investigated the correlation between the GB energy and the excess free volume for both FCC and BCC metals via atomistic simulations. Their finding suggested that GB energy and excess free volume are strictly related. Wolf [56, 57, 58] also noticed that the strength of such correlation (and therefore the scatter in the data) is strictly related to the choice of the MD potential. Cao et al. [5] argued that the moderate correlation between the GB energy and excess free volume found by Olmsted et al. [37, 38] can be improved by using by density functional theory results. Cao et al. [5] combined their own results with others available in the literature and found a strong linear correlation between GB energy and the GB excess free volume. Therefore, it is reasonable to correlate the GB excess free volume to the GB energy. In this work will use the GB energy as a surrogate of the GB excess free volume to determine GB material property.

Ratanaphan et al. [43] performed a similar calculation to [37, 38] but for two body centered cubic crystal materials (*Fe* and *Mo*) and for 408 different GBs. The five parameters GB space was divided to favor low index GBs but to also include a few ( 30%) high index boundaries. The dataset including the five parameters GB character and the corresponding calculated GB energy are available for use as supplementary material of [43]. This dataset will be used in the remainder of this chapter as the basis to calculate and assign crystallographic dependent GB properties. Figures 4.1(a) and (b) depicts the distribution of GB energy obtained by Ratanaphan et al. [43] as function of the disorientation angle and  $\Sigma$  value, respectively, for BCC Fe. Highlighted data represents  $\Sigma 3$  GBs. The  $\Sigma$  value of a GB represents the inverse of the number of coincident site lattice (CSL) points between the two adjacent crystals [42]. Neither the disorientation angle nor the  $\Sigma$  value of a CSL GB directly

correlate to the its energy.

Patala and Schuh [39] proposed a methodology to identify the fundamental zone <sup>1</sup> of each CSL GB. Specifically, given a disorientation (axis and angle) they identified the space including all the possible GB normals that can exist. Homer et al. [18] analyzed the results obtained in [37, 38] for *Ni* and *Al*. Homer et al. [18] computed the fundamental zone of each GB and investigated the correlation between the GB properties and the GB normal orientation. They found the GB energy is an almost monotonic function of the misalignment between the GB plane normal and the disorientation axis. Specifically, they observed that for GBs with a normal aligned with [100] and [111] axis the GB energy decreases monotonically while moving from a pure twist GB towards a pure tilt GB. The opposite was observed for GB with normal aligned with [110] axis.

Tschopp and McDowell [53] investigated the effect of the orientation of GB normal for  $\Sigma 3$  GBs. They defined the *inclination angle*,  $\Psi$ , as the relative rotation of the GB plane around the tilt axis. The *inclination angle* was defined to exhibit a zero value for the  $\Sigma 3$  minimum energy configuration (i.e. pure twist, coherent twin boundary) and a value of  $90^\circ$  for the  $\Sigma 3$  maximum energy configuration (i.e. pure tilt, symmetric incoherent twin boundary). They also proposed an interpolating function based on the inclination angle to compute the energy of  $\Sigma 3$  GB with a generic GB inclination angles  $\Psi$  as

$$E(\Psi) = E_{CTB} \cos \Psi + E_{SITB} \sin \Psi \quad (4.1)$$

where the subscripts *CTB* and *SITB* stands for coherent and symmetric incoherent twin boundary, respectively. In this work we extend the definition of inclination angle given by Tschopp and McDowell [53] to be independent from the GB CSL ( $\Sigma$ ) character and directly related to the GB fundamental zone as

$$\Psi = \tan^{-1} \left( \frac{\alpha_T}{\alpha_{TW}} \right) \quad (4.2)$$

where  $\alpha_T$  and  $\alpha_{TW}$  are the tilt and twist angle of a generic GB. The angle  $\Psi$  defines the orientation of the *disorientation axis* relative to the GB normal. Therefore,  $\Psi = 0^\circ$  identifies a pure twist GB and  $\Psi = 90^\circ$  identifies a pure tilt GB. All the values in between these two extremes represent a mixed character GB. However, not all the CSL GBs present in the database have been evaluated for the lowest and maximum energy configuration therefore Eq. 4.1 cannot be used to interpolate the GB energy. To overcome this issue, a best-fit polynomial interpolation will be used in this work.

Han et al. [16] investigate the correlation between the *inclination angle* and the GB sink efficiency in pure *Cu* by measuring the width of the void-denuded zone (i.e. the region of material without voids in proximity of a GB). Results show that the width of void-denuded zone is almost  $0\text{ nm}$  for a pure twist  $\Sigma 3$  GB and monotonically increases as the GB moves towards a pure tilt  $\Sigma 3$  GB. Figure 4.2(a) is a direct comparison between the GB energy and void denuded zone width for FCC. The behavior of BCC materials is complementary to the one of FCC materials [21], exhibiting the lowest energy for pure tilt in the case of  $\Sigma 3$  GB. Using this FCC-BCC duality, the GB sink efficiency data obtained by Han et al. [16] for *Cu*

---

<sup>1</sup>a fundamental zone is smallest subset of the entire space required to represent the character of a GB

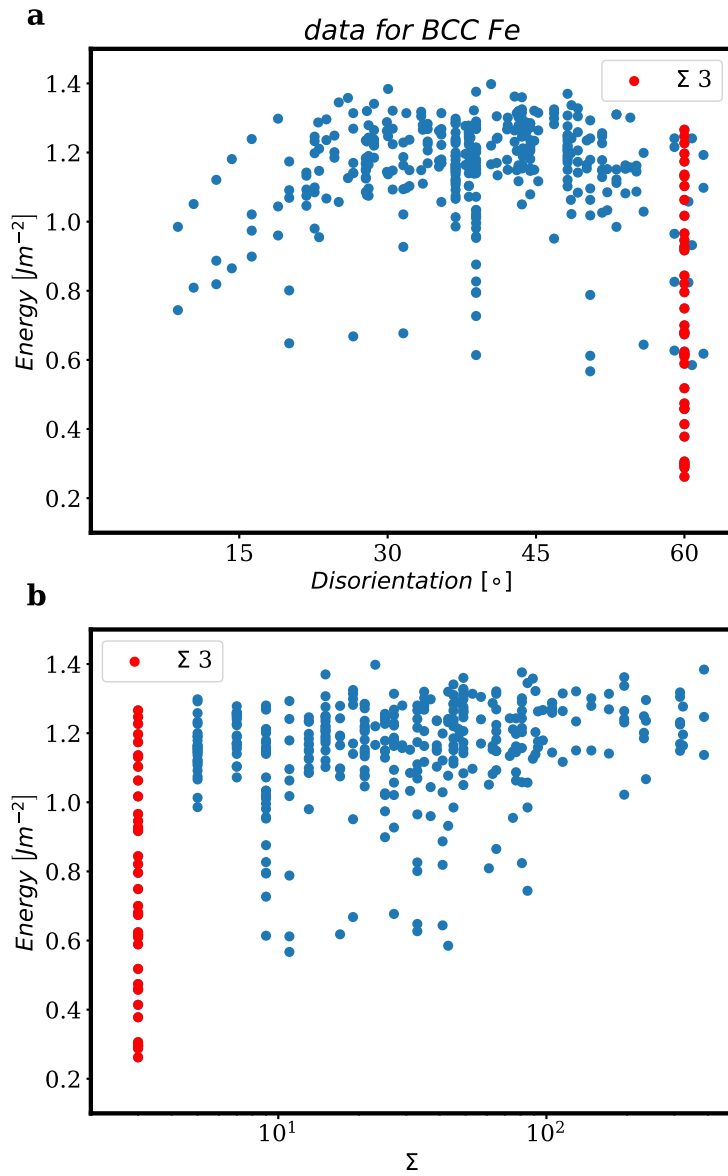


Figure 4.1: Grain boundary energy for BCC *Fe* as function of disorientation angle (a) and  $\Sigma$  value (b). Highlighted values of GB energy for all the simulated  $\Sigma 3$  GBs. Data from [43]

can be correlated to the GB energy of BCC *Fe* by using the reciprocal of the inclination angle defined as

$$\Psi^* = |90^\circ - \Psi| \quad (4.3)$$

Figure 4.2(b) depicts the results of this comparison showing the same trend exhibited in 4.2(a). Given the results of Tschopp and McDowell [53], Han et al. [16], Homer et al. [18] and the observations for Figure 4.2(a) and (b) the energy of GB that can be classified as a low  $\Sigma$  GB will be approximated as a function of the  $\Sigma$  value and the inclination angle as defined in Eq. 4.2.

For each value of  $3 \leq \Sigma \leq 99$  the available GB energy data are used in conjunction with the definition of *inclination angle* (Eq. 4.2). For each sigma value four best-fit polynomial approximations (constant through third order) are generated and manually checked to select the most appropriate. Figure 4.3 depicts an example of approximating the GB energy of  $\Sigma 3$  GBs with the inclination angle. In this case the third order polynomial was selected as best approximation. This procedure is applied to all CSL GBs available in the database. The best-fit polynomial is then used to represent the energy of each CSL GB for  $\Sigma \leq 99$ .

#### 4.1 Correlating the GB energy to five parameters grain boundary space

We adopt the following interpolation scheme to correlate the five GB parameters to GB energy. First, of all each of the 695 GB present in the RVE need to be classified either as a CSL or random GB. Because low energy GBs (e.g. GB energy lower than  $0.8\text{J/m}^2$ ) are observed only for  $\Sigma \leq 99$  we will first limit the classification to this range (see Fig. 4.2(b)).

Figure 4.4(a) shows the results of the classification procedure. The black line represents the distribution of GB disorientation angle, which is very close to the theoretical GB disorientation distribution calculated by Mackenzie [28]. This shows that RVE is large enough to represent the actual random GB disorientation distribution. Figure 4.4(b) shows the area weighted distribution for each CSL GB found in the RVE. As one would expect, the most common CSL GB is  $\Sigma 3$ , with an area fraction just over 3%. Other common GBs are  $\Sigma 5, 9, 11$  with area fractions just above 1%. These area fractions are in good agreement with the theoretical predictions of Morawiec et al. [33] for a material exhibiting a random texture.

For all the grain boundaries that are classified as random GB we assume a bilinear dependence of the GB energy as function of the disorientation angle: for a disorientation angle  $0^\circ < \theta \leq 22^\circ$  the energy is assumed to vary linearly from 0 to  $1.22\text{Jm}^{-2}$  while for  $\theta \geq 22^\circ$  the GB energy is assumed to be equal to  $1.22\text{Jm}^{-2}$ . Furthermore, because the lack of data in the literature about the energy of random GB some random variance has also been assumed. In the final model, the random GB energy is drawn from a normal distribution centered about the mean bilinear model and with variance varying linearly from 0 to  $0.05\text{Jm}^{-2}$  for  $0^\circ < \theta \leq 22^\circ$  and equal to  $0.05\text{Jm}^{-2}$  for  $\theta \geq 22^\circ$ . This distribution envelopes the energy for random GBs is depicted in Figure 4.5, compared to the data available from [43].

Figure 4.6(a) depicts the energy assigned to all the GBs present in the RVE. Many high angle CSL GBs exhibit energy values much lower than random GBs. The GB showing the lowest energy is a low-disorientation random GB. For CSL GBs, the lowest energy value is obtained for a disorientation of  $60^\circ$  (i.e.  $\Sigma 3$  GB).

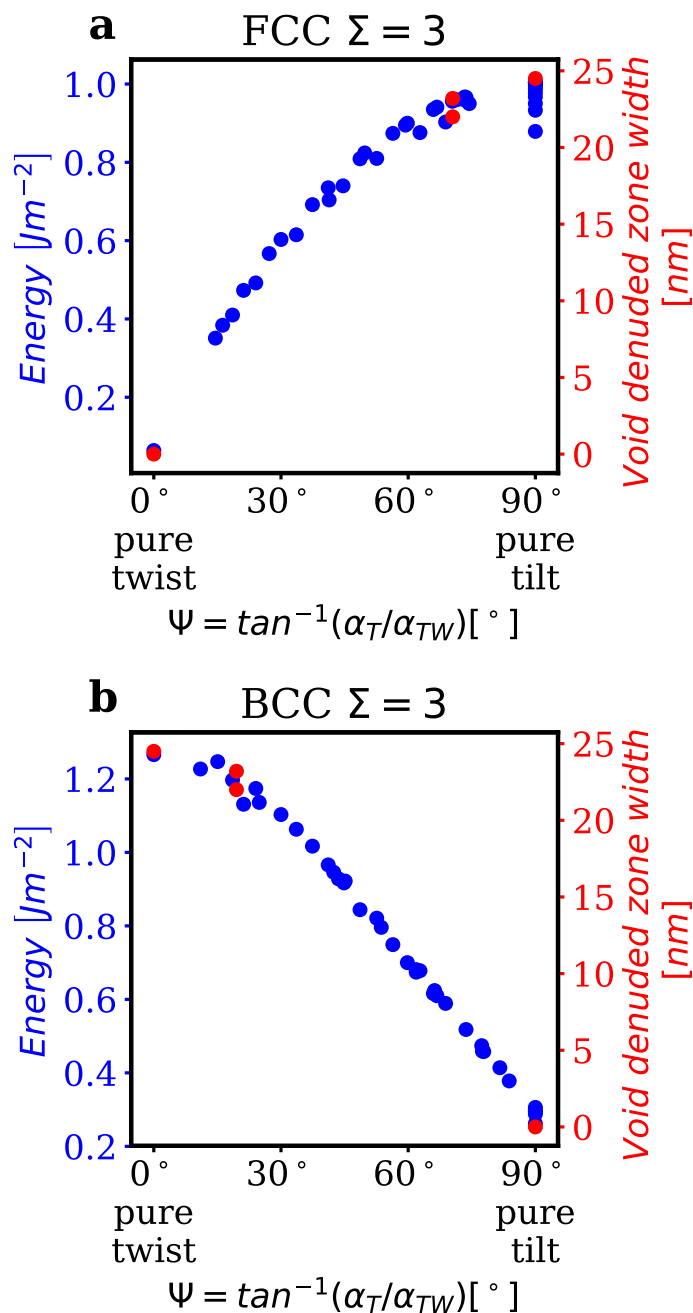


Figure 4.2: (a) Comparison of  $\Sigma 3$  GB energy (Ni) and void denuded zone width (Cu) as function of the inclination angle. GB energy (blue points) data from [37] and void-denuded zone (red points) data from Han et al. [16] (b) Comparison of  $\Sigma 3$  GB energy (Fe) and void denuded zone width (Cu) as function of the inclination angle. Note that void denuded zone data have been plotted using Eq. 4.3. GB energy data from [43].

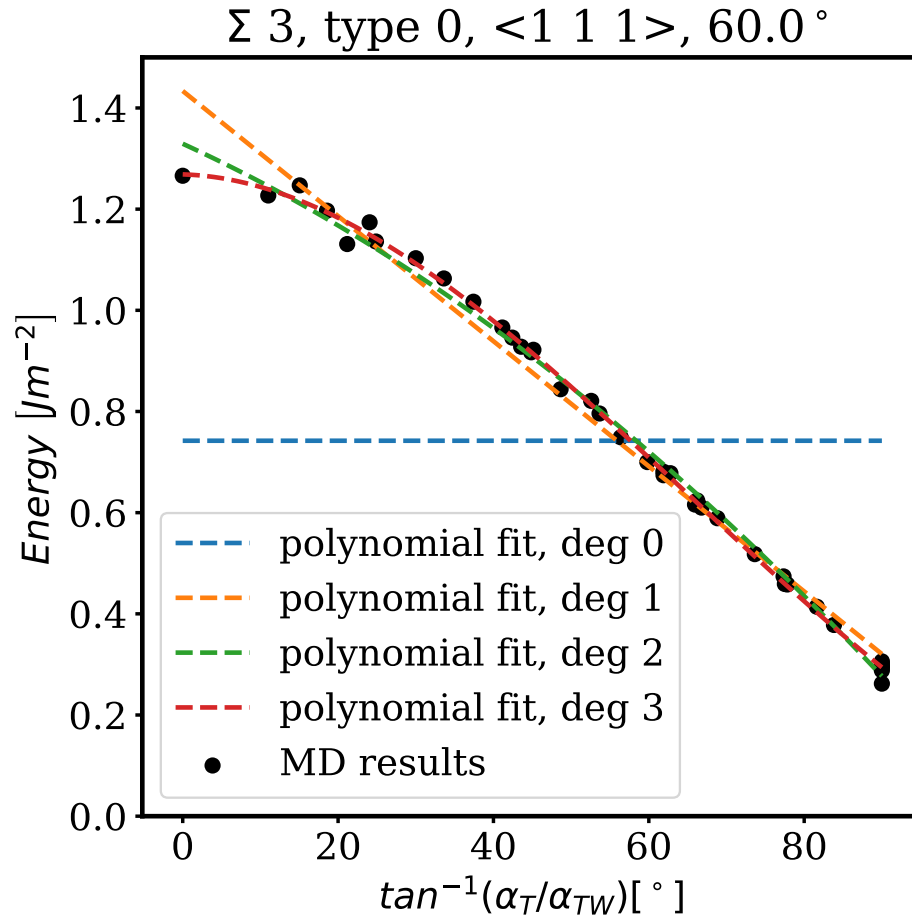


Figure 4.3: Interpolation of the energy of  $\Sigma 3$  GBs with respect to the inclination angle  $\Psi$  using different polynomial orders.

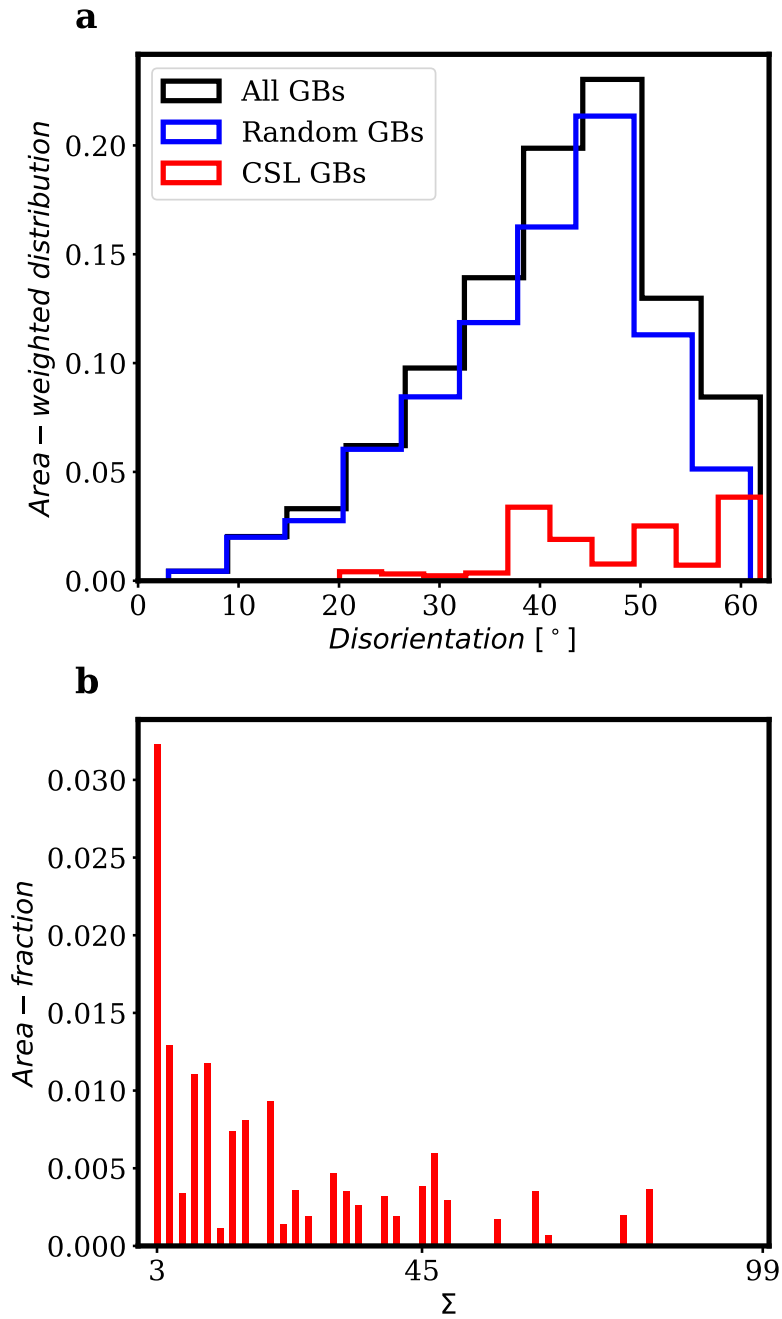


Figure 4.4: (a) Area-weighted disorientation distribution of the GBs present in the RVE. The contribution of random and CSL boundaries is also highlighted. (b) Area fraction of CSL GB for each  $\Sigma$

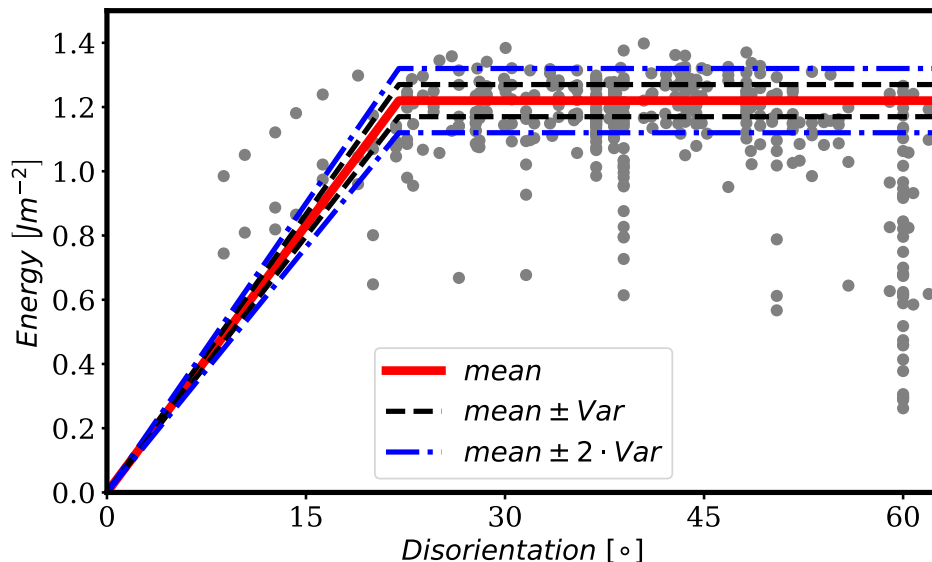


Figure 4.5: Comparison of the distribution of the energy of random GBs against data available from [43]

Figure 4.6(b) shows the area-weighted distribution of GB energy. The contribution of random and CSL GBs to the overall energy distribution is also shown.

## 4.2 Choosing GB properties as functions of GB energy

The GB energy can be interpreted as a measure of the disorder of the crystalline structure. As described above, the GB energy is a good first-order correlator of the GB excess free volume.

The task of this subsection is to select values of the GB parameters used in the physical interface-cohesive model, described in Chapter 3. The GB deformation model has eight physical parameters which are summarized in Table 4.1.

The GB sink efficiency is proportional to the GB free volume and it is directly related to the GB diffusivity. Intuitively, vacancy diffusion inside a GB is easier when a higher free volume is available. Therefore, the GB diffusivity,  $D_{GB}$ , is assumed to be proportional to the GB energy (e.g. higher energy, higher the diffusion coefficient). The GB viscosity,  $\eta_{GB}$ , is inversely related to the GB diffusivity [14] (see Eq. 3.4).

Tschopp et al. [54] studied the correlation between mean vacancy formation energy and the GB energy in  $\alpha - Fe$ , finding an inverse correlation between the two variables. This means that vacancy formation should scale with GB energy. Therefore, as a first order approximation, we will assume the nucleation rate  $F_N$  to be directly related to the GB energy. The nucleation stress,  $\Sigma_0$ , and the nucleation exponent,  $\beta$ , should also scale according to the GB energy. However, as a first approximation we keep these parameters constant and rely on the nucleation rate to capture the physical scaling of void nucleation with GB character.

There are few studies describing the distribution of the initial cavity radius,  $a_0$ , and

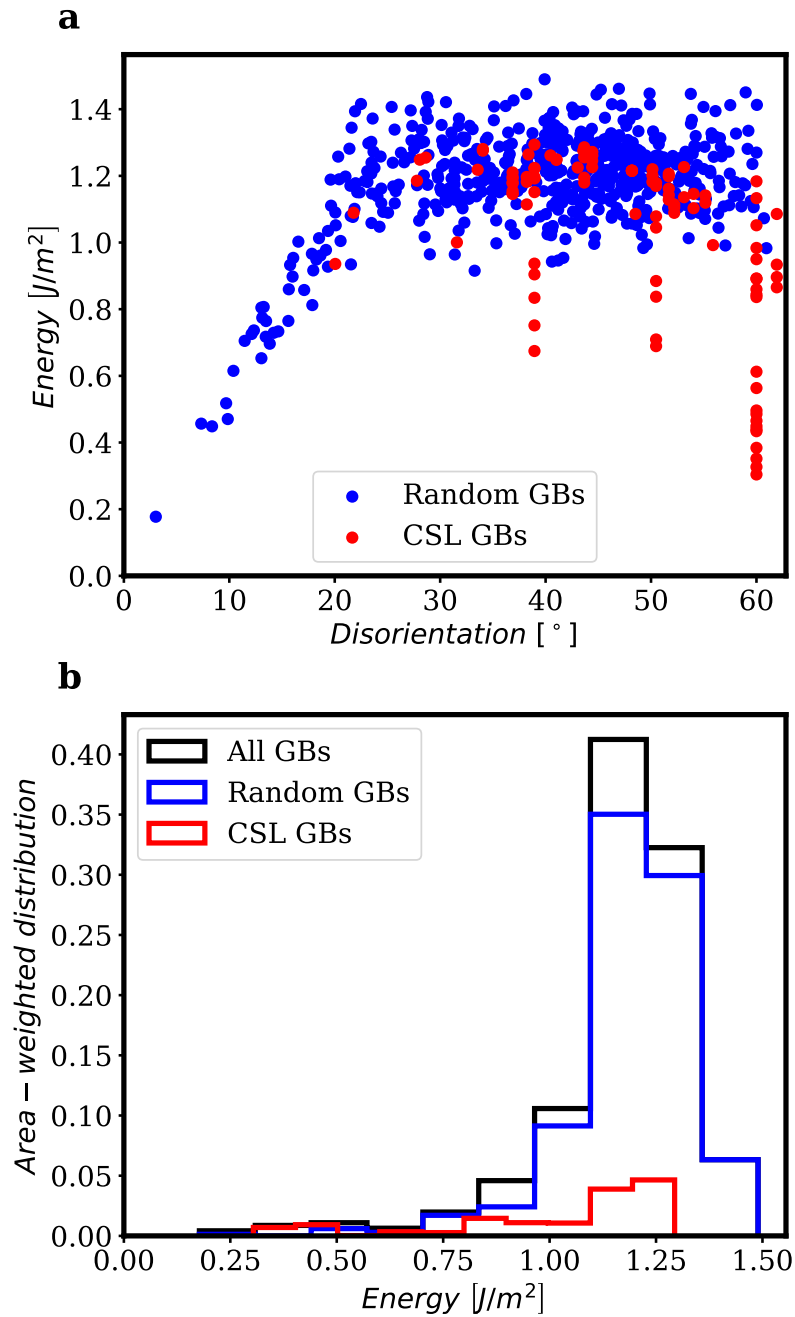


Figure 4.6: (a) Energy of GBs present in the simulate RVE against disorientation angle; (b) Area-weighted distribution of GB energies normalized against the total GB area) [43]

Property	Symbol	Crystallographic?	Scaling
GB viscosity	$\eta$	Yes	$\propto E_{GB}^{-1}$
Initial cavity radius	$a_0$	No	-
Initial cavity spacing	$b_0$	No	-
GB diffusivity	$D_{GB}$	Yes	$\propto E_{GB}$
Cavity half-angle	$\psi$	No	-
Nucleation stress	$\Sigma_0$	No	-
Nucleation rate	$F_N/N_I$	Yes	$\propto E_{GB}$
Nucleation exponent	$\beta$	No	-

Table 4.1: Decisions in the model on how to scale the GB parameters with GB energy ( $E_{GB}$ ).

cavity spacing,  $b_0$ , as function of the GB character (see for instance [16]). The few data available in the literature are scattered and do not show a strong correlation between the GB character and the initial void spacing and size. Therefore,  $a_0$  and  $b_0$  are constant in this model and do not scale with the GB energy.

The last model parameter is the cavity half-angle,  $\psi$ , which is geometrical parameter related to the shape of void. This parameter is kept constant as it can be considered independent from the GB character at CPFEM length scale.

To instantiate simulations and obtain a fair comparison between the model proposed in this section and the original model with constant GB properties the distribution of each parameter need to be scaled appropriately. The scaling approach used hereafter keeps the area averaged crystallographic-dependent GB property,  $P_{AVG_{GB}}$ , equal to the constant GB property,  $P_{AVG}$ , used in the original model. This can be stated in mathematical term as:

$$P_{AVG} = P_{AVG_{GB}} = \frac{1}{A_{tot}} \sum_{i=1}^{N_{gb}} P_i \cdot A_i \quad (4.4)$$

where  $A_{tot}$  is the total GB area,  $N_{gb}$  is the total number of GBs present in the RVE, the subscript  $i$  is an index representing a GB and  $P$  and  $A$  are a generic material property and the area of  $i$ -th GB, respectively.

With the relationship between the GB energy and each GB property defined, the only task left is assign the appropriate property range. In what follows we will assume a range of variation of each property of two orders of magnitude. This range is based on the results in Chapter 3, where the GB properties were observed by scale by about this much over a temperature range of 300° C. Furthermore, because the GB energy is not evenly distributed across the RVE, an optimization procedure is used to impose the selected range of variation while enforcing the equivalence of the mean property value (e.g. Eq. 4.4).

Figures 4.7(a), (b), and (c) depict the area weighted distribution of the GB diffusivity, viscosity and nucleation rate obtained by using the proposed approach. Vertical red lines represent the location of the obtained maximum, minimum and mean value of the GB properties. The actual values can be found in the plot legends. In all the distributions only a small fraction of GBs exhibits property far from the mean value. The extreme values (e.g. the imposed Max/Min) cannot be seen in the plot because they belong to only to one GB.

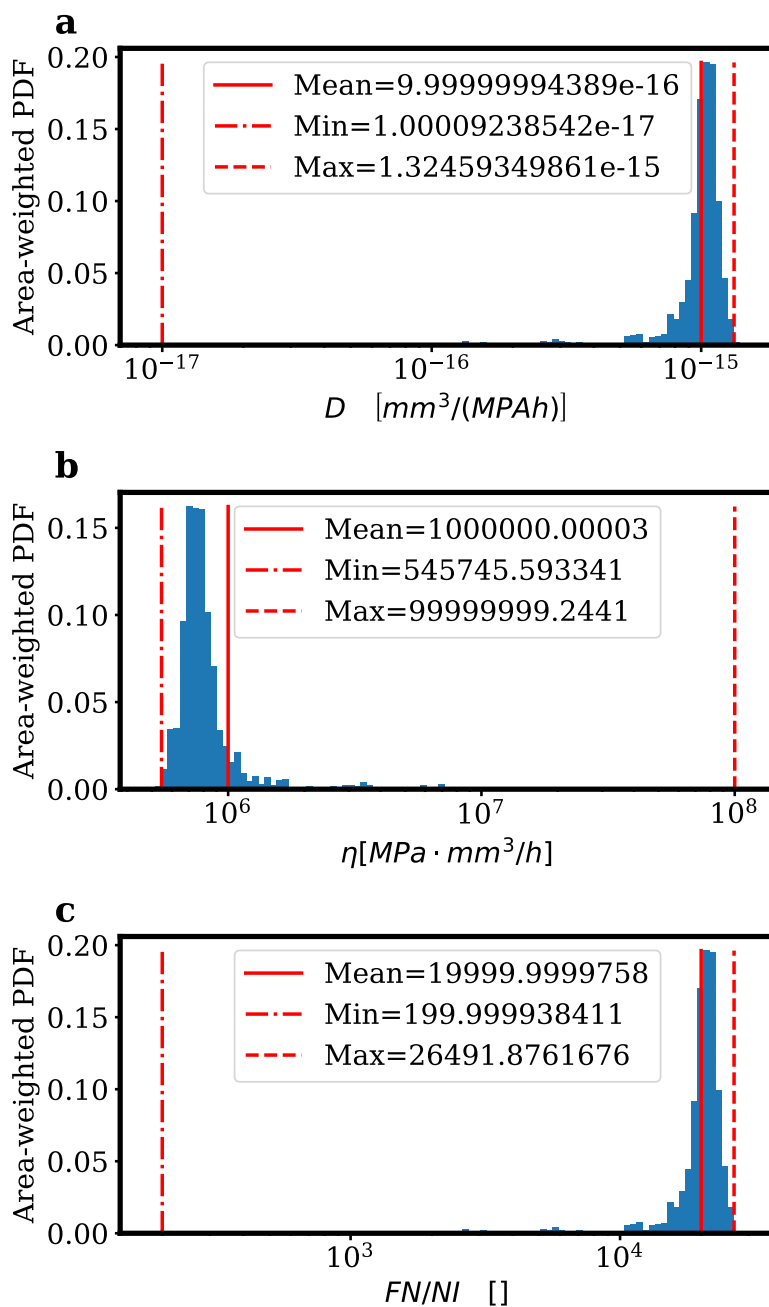


Figure 4.7: Comparison of the distribution of GB properties obtained for 600° C using the GB energy model and a two order of magnitude property range: (a) GB diffusivity, (b) GB viscosity, (c) Nucleation rate

Property	Symbol	Scaling	Mean Value	Imposed Min/Max	Units
GB diffusivity	$D_{GB}$	Direct	$1e-15$	$1e-17$	$MPa^{-1} \cdot hr^{-1} \cdot mm^3$
GB viscosity	$\eta$	Inverse	$1e6$	$1e8$	$MPa \cdot hr \cdot mm^{-1}$
Nucleation rate	$F_N/N_I$	Direct	$1e4$	$1e2$	Unknown

Table 4.2: Mean value and imposed range of the crystallographic GB properties.

### 4.3 Assessing the effect of crystallography-depedent grain boundary properties

The net effect of varying GB properties with the GB energy is to strengthen low energy GBs and to weaken high energy GBs. A small fraction of GB will become much more resistant to GB cavitation compared to the average properties in the previous simulations while most of the GBs will become slightly more compliant. However the resulting microstructure will still exhibit the same average GB properties. If creep rupture is weak link phenomenon in which the weakest/stronger GB plays a significant role then the new simulations, which take into account GB crystallography, should capture this behavior showing a different macroscopic response. On the other hand, if creep rupture is not a weakest link phenomenon then we should not see much macroscale difference between the two types of simulations, as both simulations have the same average, macroscale properties.

Three pairs of simulations were used to examine the effect of including crystallographic dependent GB properties. For each of the condition described in Table 4.4 one simulation uses, fixed mean GB material properties (as in Table 3.2) and another simulation uses crystallographic dependent GB properties. To compare results at the macroscopic length-scale and better understand the influence of the different mechanism, the *total creep rate* has been partitioned into different contributions as follows:

- Total Creep rate
  1. Grain Creep rate
    - (a) Grain Elastic
    - (b) Grain Plastic
    - (c) Grain Diffusion
  2. GB Creep rate
    - (a) GB Opening
    - (b) GB Sliding

The above quantities have been computed for both the effective creep rate (using the von Mises effective strain) and the creep rate aligned with loading direction.

Figures 4.8, 4.9 and 4.10 depict the comparison of the decomposed effective strain rate for 60, 100, and 140 MPa applied uniaxial loads. Figures 4.11, 4.12 and 4.13 depict the same results but for the strain rate component aligned with the loading direction. Only very small differences occur when comparing the in the macroscopic results for the two types of models. The differences occur between the beginning of the simulation and a model time of

Simulation	Stress level	Simulation time to breakdown	
		Standard	New
#1	60 MPa	201734.064 [hrs]	188240.006 [hrs]
#2	100 MPa	39733.8335 [hrs]	42604.6018 [hrs]
#3	140 MPa	4674.68963 [hrs]	3949.27874 [hrs]

Table 4.3: Comparison of simulation time to breakdown between the standard and crystallographic dependent GB model for different stress levels at 600° C

10 hrs. Very small differences are observed for all the deformation mechanisms except for bulk diffusion.

However, at some point between 10 and 100 hrs the differences between the response of the two models almost vanishes. At the beginning of primary creep the standard model show lower creep rate than the GB sensitive one. The higher diffusivity and lower viscosity of almost half of the GB population (see 4.7) enhances the overall GB sliding contribution. After approximately one 1 hr the trend reverse and the overall GB creep rate of the standard model becomes higher. At this point the effect of GBs with higher viscosity and lower diffusivity becomes relevant. The stronger than average GBs impose higher cohesive tractions thus preventing additional opening and sliding. This mechanism prevents the weak GBs from continuing to sliding, thus lowering the overall GB contribution to the creep rate. Then, somewhere in between 10 and 100hrs the stronger than average GBs start slowly accumulating damage. Because most of the stronger GBs have properties close to the mean their effect on the overall creep behavior is small and lasts only until some damage is accumulated and their properties start to degrade. At this point the mean property GBs starts to dominate and the behavior of the two models almost coincide.

Both types of creep rupture simulations (mean and distributed properties) eventually numerically fail. The model time to breakdown of the three pairs of simulations is summarized in Table 4.3. There is an almost 10% difference between the model time to breakdown of each simulation pair. Furthermore the simulation breakdown happens at a lower model time for the crystallographic dependent GB property model for Simulations #1 and #3 while the original model breaks down earlier for Simulations #2. Simulation breakdown could be caused by the actual failure of the RVE (e.g. the RVE is so damaged that it cannot withstand the imposed load) or from some numerical issues unrelated to a physical mechanism. Grade 91 usually has reasonable creep ductility, accumulating a large amount of strain in tertiary creep before failure [19]. The current CPFEM model fails before this behavior can occur. Larger differences between the two models might accumulate over this final stage of creep.

Microscale results of the distributed-property GB model suggest that GB engineering might be employed to improve the creep performance of Grade 91. Figures 4.14, 4.15 and 4.16 compares the behavior of the five strongest GBs at different simulated times with a stress level of 60MPa. The model times have been selected to show onset of damage in the standard model (Fig. 4.14), in the microstructural sensitive GB model (Fig. 4.15), and at simulation breakdown (Fig. 4.16). The color scale represents the normalized cavity radii. Approximately at approximately 13,000 hours one of the favorably oriented GB starts

Simulation	stress state	stress value	Temperature
#1	Uniaxial Tension, Z-axis	60 MPa	600 °C
#2	Uniaxial Tension, Z-axis	100 MPa	600 °C
#3	Uniaxial Tension, Z-axis	140 MPa	600 °C

Table 4.4: Mean value and imposed range of the crystallographic dependent GB properties.

cavitating in the standard model. The same amount of cavitation for the same GB is reached approximately after approximately 137,000 hrs and in the standard model the normalized cavity radii is more doubled. At simulation breakdown the tracked GB shows a more than 100% difference in cavity radii. This is evidence that the creep behavior of Grade 91 could be improved by increasing the number of low-energy GB.

Summarizing the results of this chapter, including crystallographic dependent GB properties is not required to capture the average macroscopic behavior of an RVE of untextured Grade 91. This also implies that the creep behavior of Grade 91 is mainly driven by the average GB properties, at least up to just after the onset of tertiary creep. After this time the current simulations break down. Further work is needed to ascertain the effect of crystallographic dependent GB properties on macroscopic creep ductility. Microscopic results shows that Grade 91 creep behavior could be improved by increasing the fraction of low energy GB.

## 4.4 Supplementary material: Details on the calculation of the grain boundary character

### 4.4.1 Grain Boundary Disorientation

A common way to represent a crystal lattice orientation with respect to a reference frame is to use three Euler angles  $\phi_1, \Phi, \phi_2$ . The Euler angles represents three successive rotations along some axis. There are different Euler angle conventions in crystallography. For instance, the Bunge convention assumes rotations along  $Z_{\phi_1}, X_{\Phi}, Z_{\phi_2}$ . The rotation  $\mathbf{g}(\phi_1, \Phi, \phi_2)$  required to rotate a vector  $v$  observed in the sample frame to the crystal frame is defined as  $\mathbf{g}(\phi_1, \Phi, \phi_2) = Z_{\phi_2} X_{\Phi} Z_{\phi_1}$  (e.g.  $\vec{v}_{crystal} = \mathbf{g}(\phi_1, \Phi, \phi_2) \vec{v}_{sample}$ ). The misorientation is the rotation required to rotate a vector defined in the reference system of crystal  $A$  into the reference system of crystal  $B$  and is defined as follow:

$$\Delta \mathbf{g}_{AB} = \mathbf{g}_B \mathbf{g}_A^{-1} \quad (4.5)$$

where  $\mathbf{g}_A$  and  $\mathbf{g}_B$  are the rotation matrices representing the orientation of crystal  $A$  and  $B$ , respectively. A misorientation can be represented by an angle and an axis of rotation. Assuming the misorientation is available in a matrix form, the misorientation angle  $\theta$  and the axis of rotation  $\vec{a}$  can be compute using Eqs. 4.6 and 4.7, respectively.

$$\theta = \cos^{-1} \left( \frac{\Delta \mathbf{g}_{AB}(1,1) + \Delta \mathbf{g}_{AB}(2,2) + \Delta \mathbf{g}_{AB}(3,3) - 1}{2} \right) \quad (4.6)$$

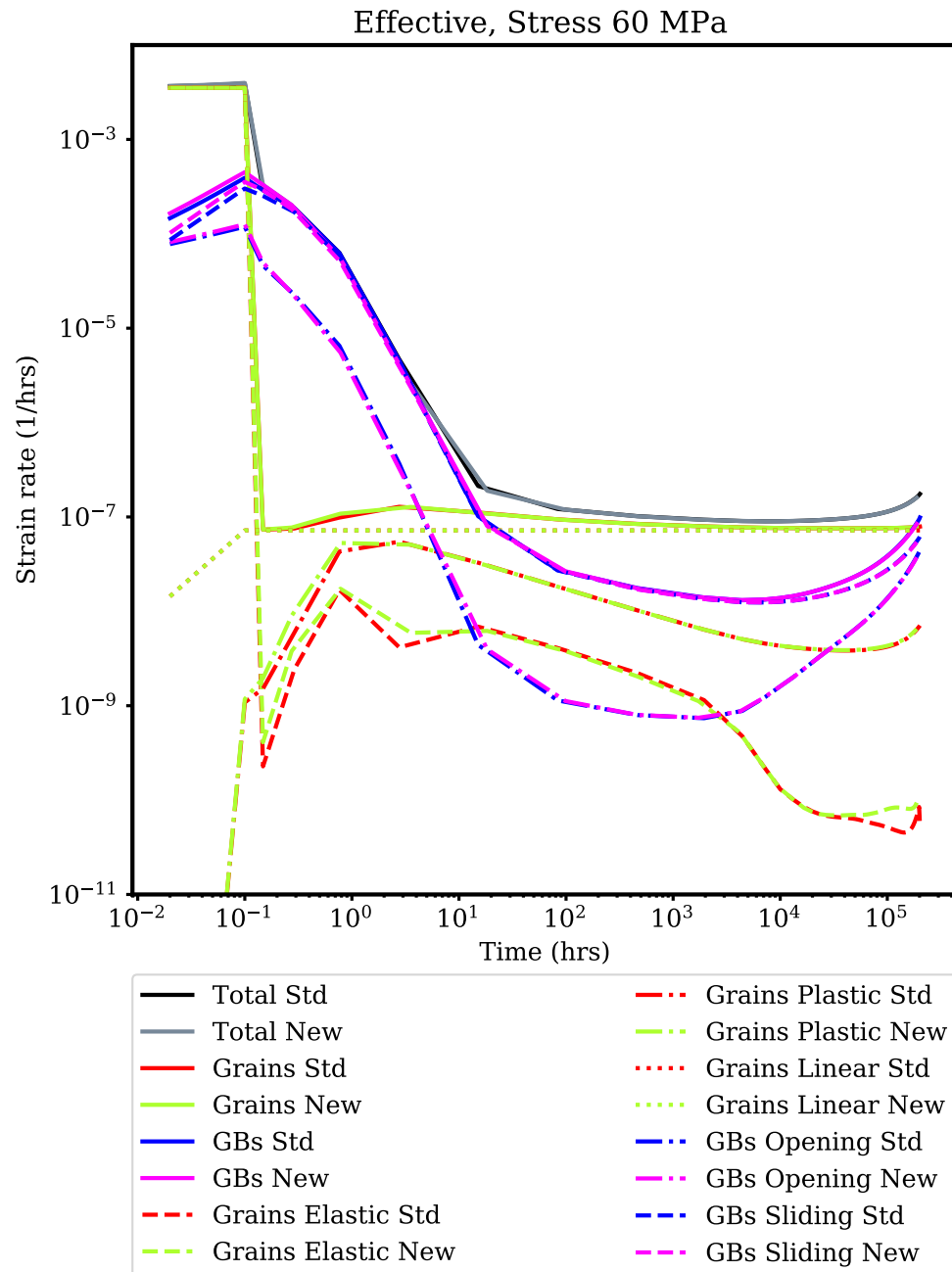


Figure 4.8: Comparison of the macroscopic cell strain rate decomposed into mechanisms within the grains and along the grain boundaries for the standard and crystallographic dependent GB models. Stress level is 60MPa.

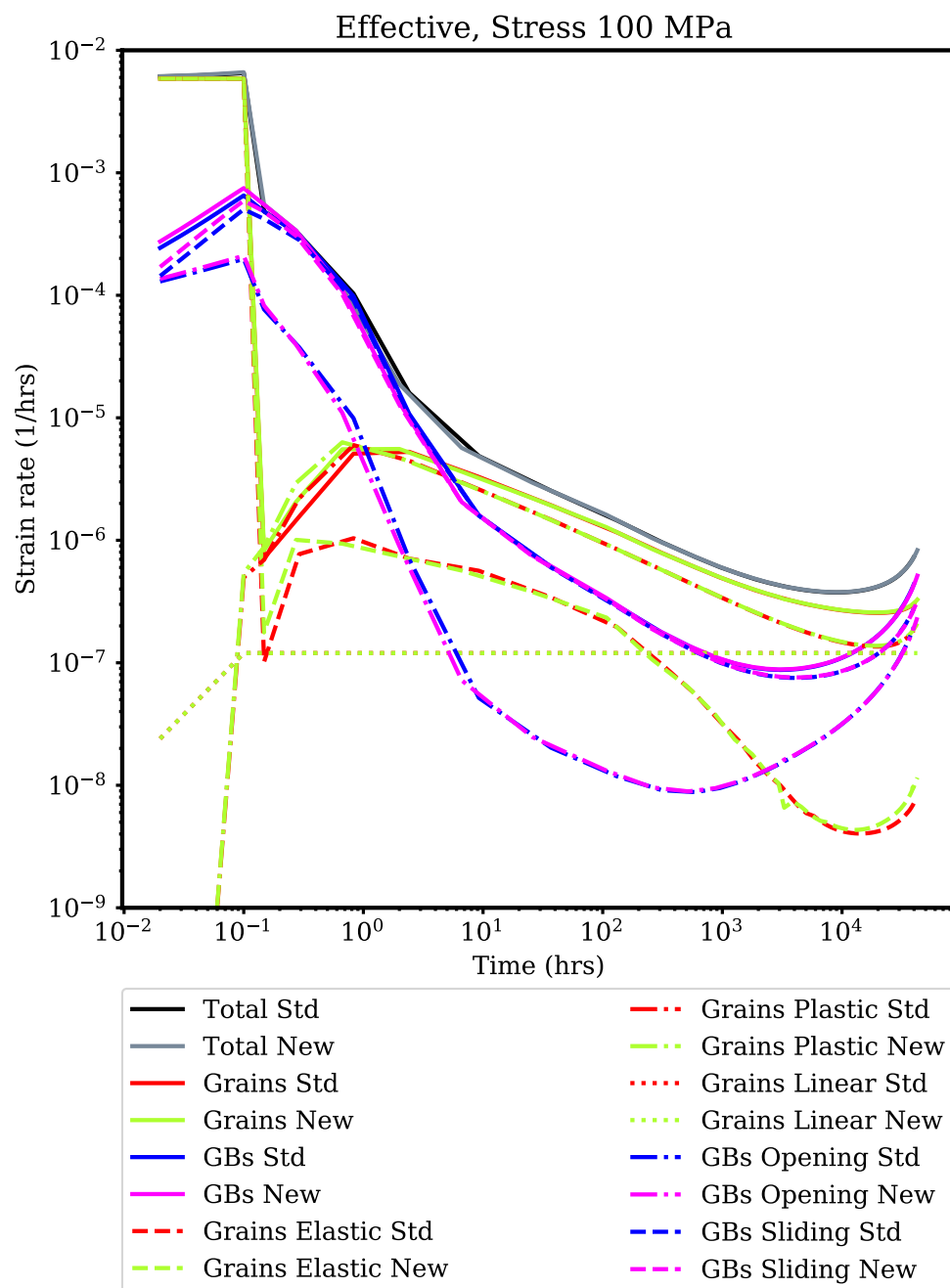


Figure 4.9: Comparison of the macroscopic cell strain rate decomposed into mechanisms within the grains and along the grain boundaries for the standard and crystallographic dependent GB models. Stress level is 100 MPa.

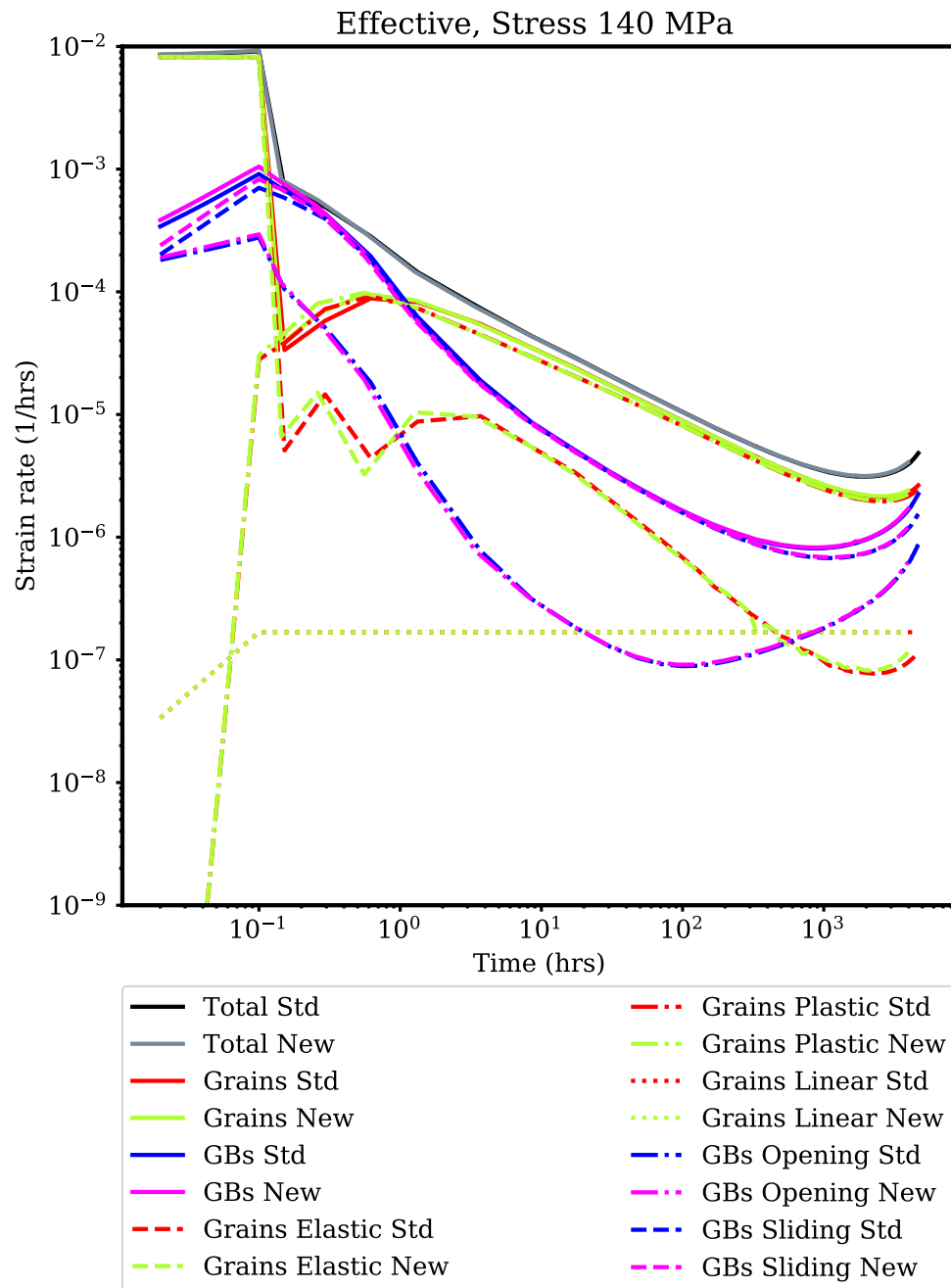


Figure 4.10: Comparison of the macroscopic cell strain rate decomposed into mechanisms within the grains and along the grain boundaries for the standard and crystallographic dependent GB models. Stress level is 140 MPa.

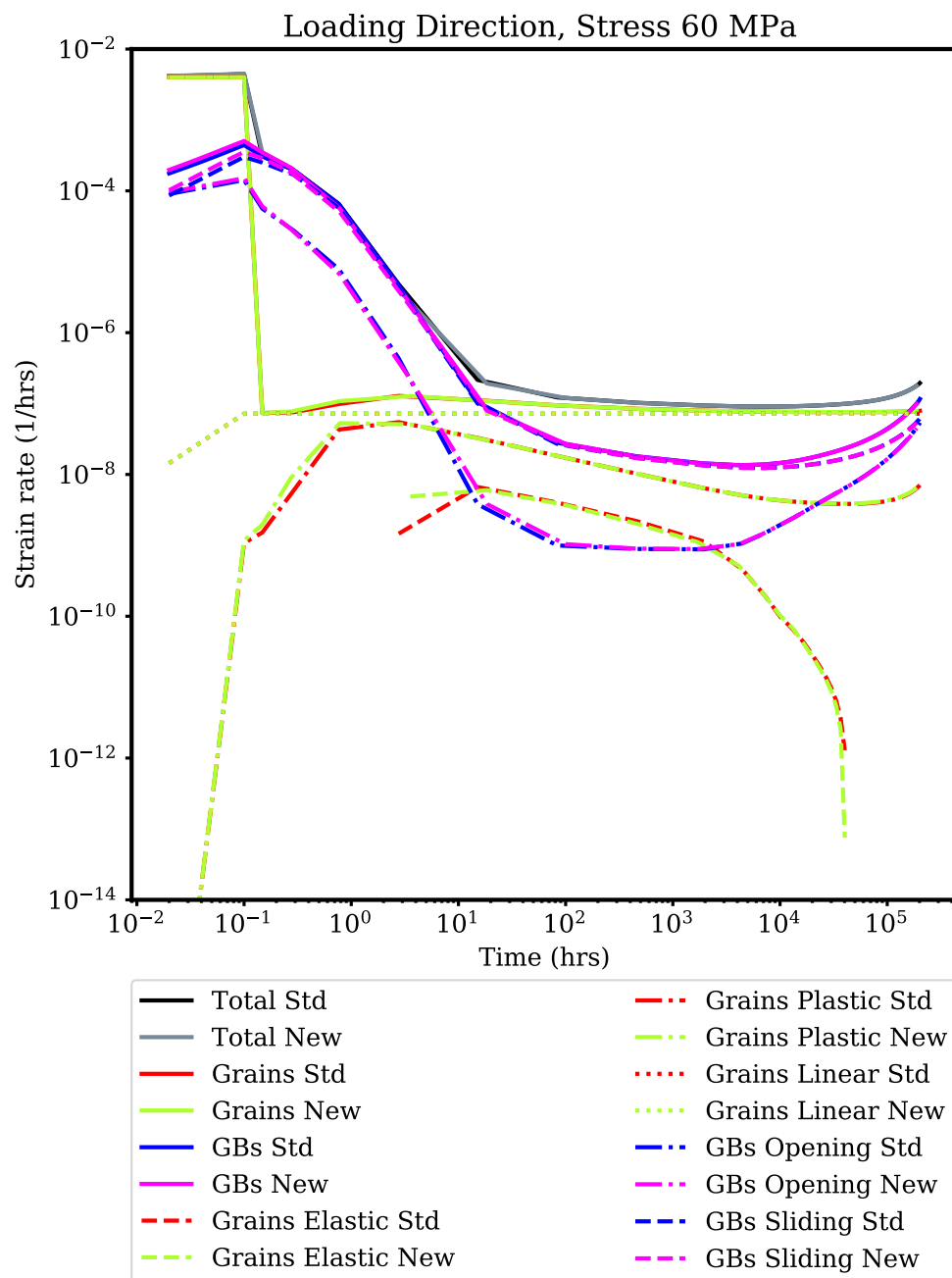


Figure 4.11: Comparison of the macroscopic cell strain rate in the loading direction decomposed into mechanisms within the grains and along the grain boundaries for the standard and crystallographic dependent GB models. Stress level is 60 MPa.

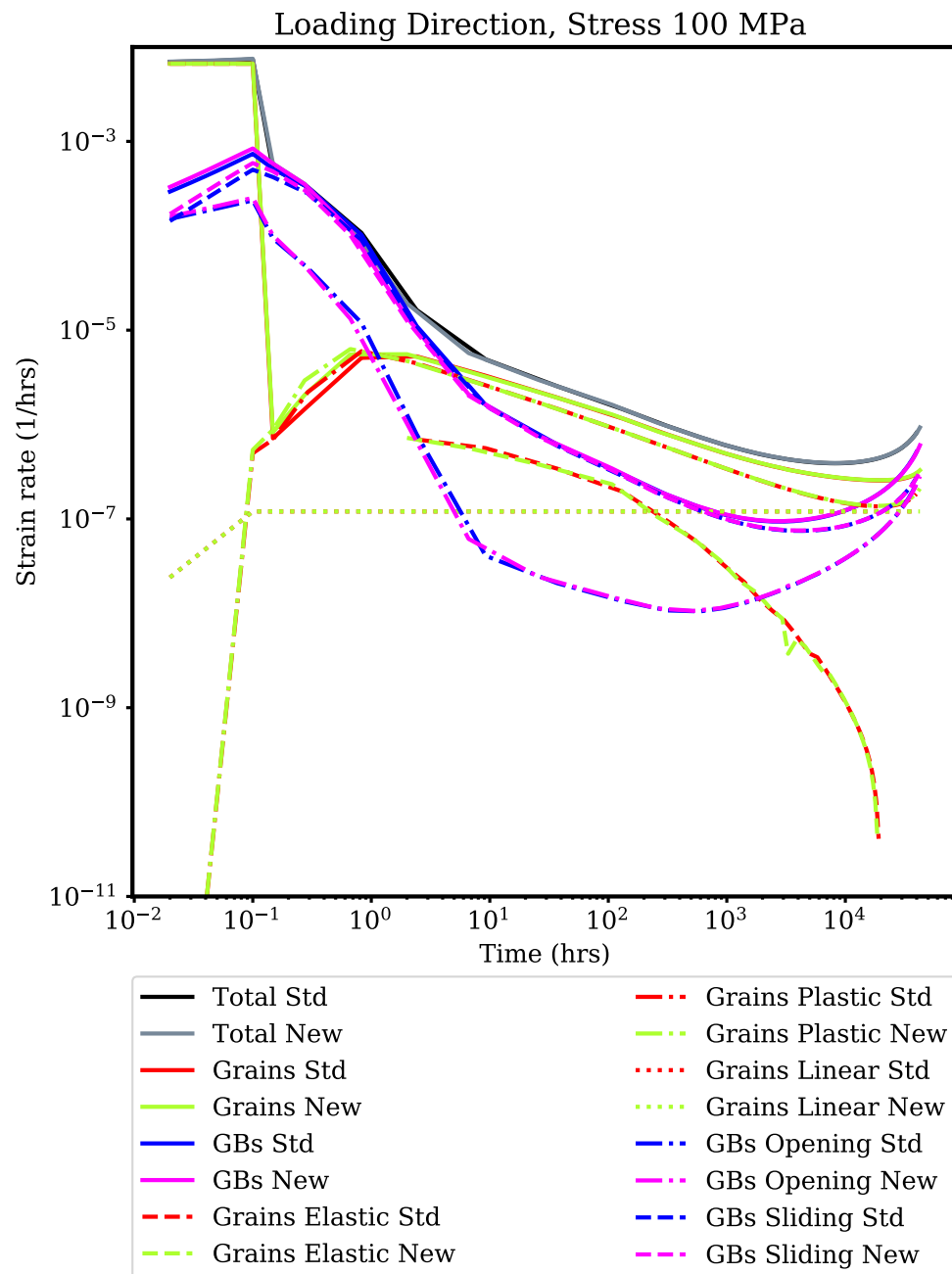


Figure 4.12: Comparison of the macroscopic cell strain rate in the loading direction decomposed into mechanisms within the grains and along the grain boundaries for the standard and crystallographic dependent GB models. Stress level is 100 MPa.

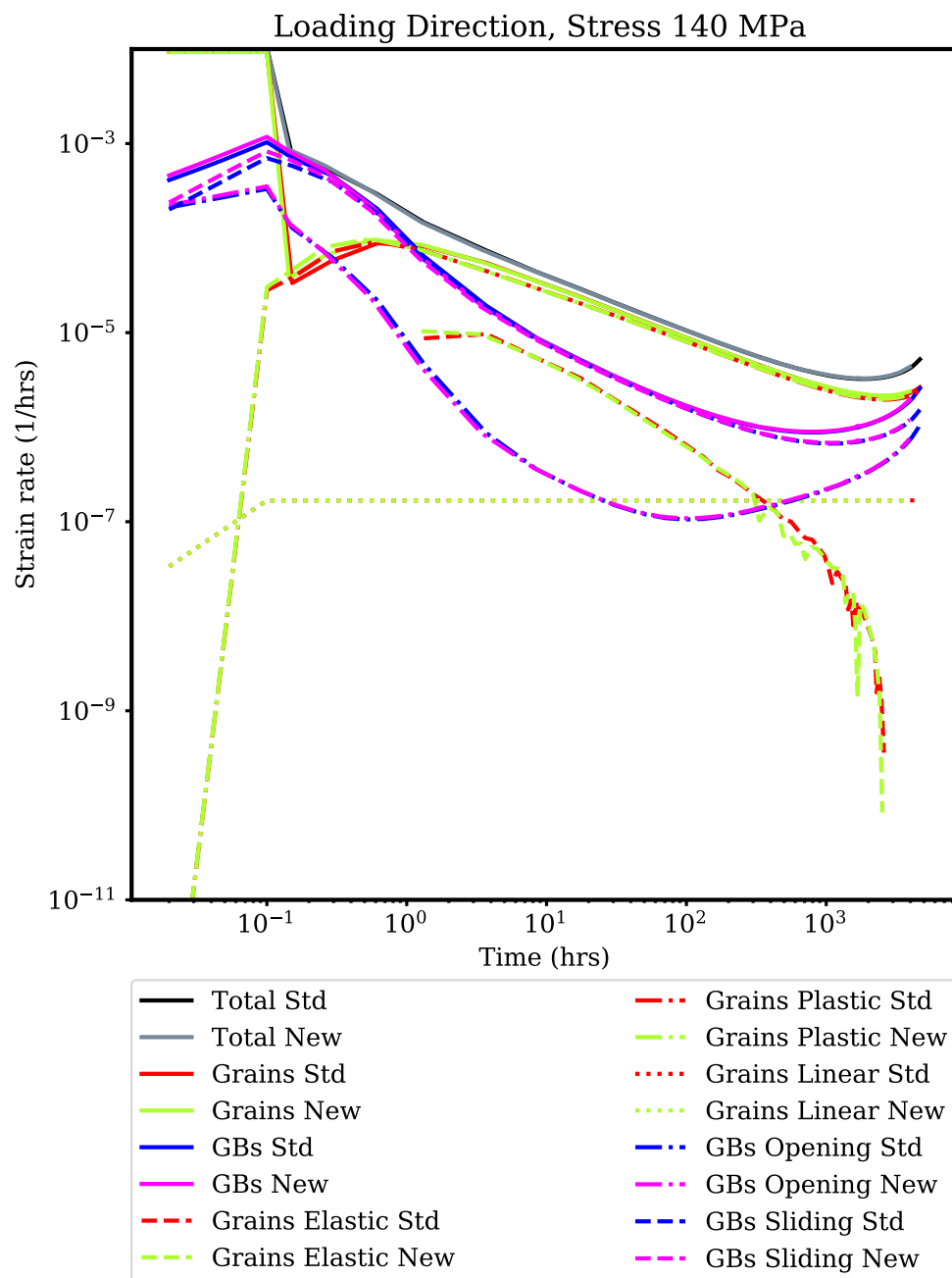


Figure 4.13: Comparison of the macroscopic cell strain rate in the loading direction decomposed into mechanisms within the grains and along the grain boundaries for the standard and crystallographic dependent GB models. Stress level is 140 MPa.

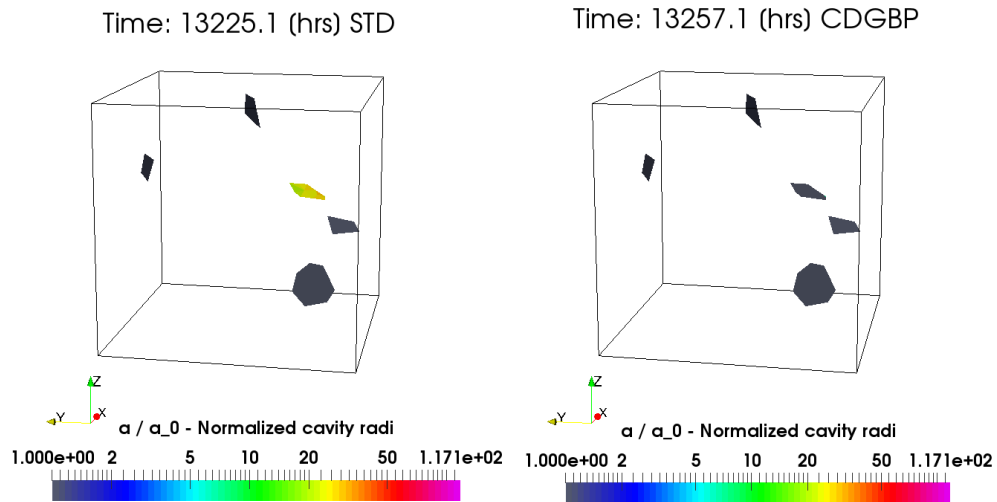


Figure 4.14: Comparison of the normalized cavity radii obtained by the two models for the five strongest GBs present in RVE. Stress level is 60MPa and the time is at the onset of damage in the standard model.

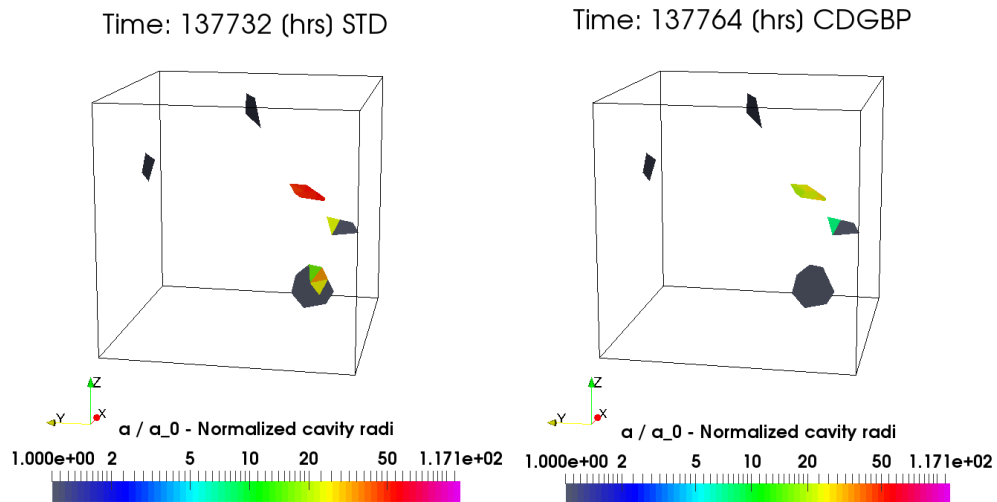


Figure 4.15: Comparison of the normalized cavity radii obtained by the two models for the five strongest GBs present in RVE. Stress level is 60MPa and the time is the onset of damage in the vary-properties model.

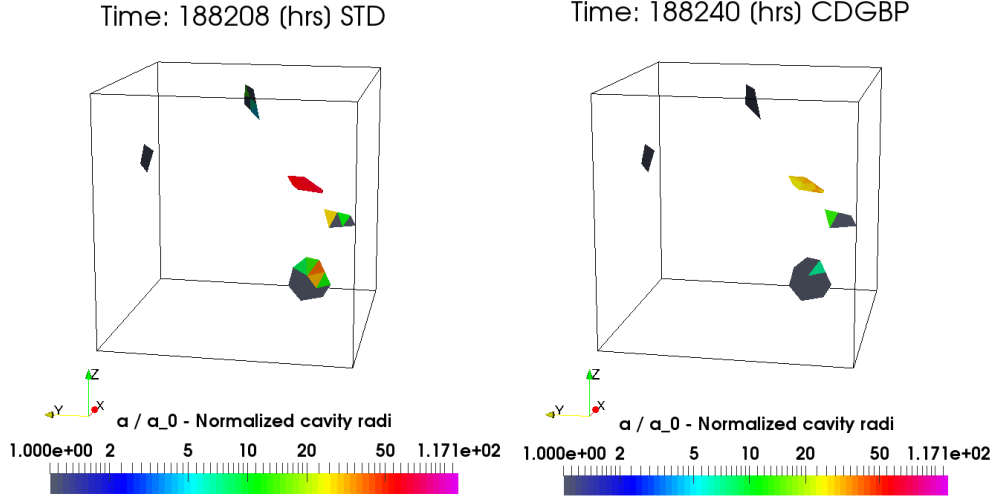


Figure 4.16: Comparison of the normalized cavity radii obtained by the two models for the five strongest GBs present in RVE. Stress level is 60MPa and the time is at simulation breakdown.

$$\begin{bmatrix} a_1 \\ a_2 \\ a_3 \end{bmatrix} = \begin{bmatrix} \Delta \mathbf{g}_{AB}(3, 2) - \Delta \mathbf{g}_{AB}(2, 3) \\ \Delta \mathbf{g}_{AB}(1, 3) - \Delta \mathbf{g}_{AB}(3, 1) \\ \Delta \mathbf{g}_{AB}(1, 2) - \Delta \mathbf{g}_{AB}(2, 1) \end{bmatrix} \quad (4.7)$$

Most crystalline solids have rotational symmetries. For instance, body-centered cubic crystals, possess 24 symmetries that will be indicated as  $S$ . Because of symmetries, a vector observed in the sample reference has 24 crystallographic equivalents, e.g.  $\vec{v}_{crystal} = \mathbf{S}_i \mathbf{g}_A \vec{v}_{sample}$  is equivalent to  $\vec{v}_{crystal} = \mathbf{S}_j \mathbf{g}_A \vec{v}_{sample}$ . The indexes  $i$  and  $j$  range from 1, ..., 24 and represent different symmetries. Because of the symmetries of both crystals, Eq. 4.5 can be rewritten as

$$\Delta \mathbf{g}_{AB,i,j} = S_i \mathbf{g}_B (S_j \mathbf{g}_A)^{-1} \quad (4.8)$$

Furthermore, the misorientation of a GB, must be independent from the reference grain, i.e.  $\Delta \mathbf{g}_{AB}$  must be equivalent to  $\Delta \mathbf{g}_{BA}$ . This means that the misorientation of grain boundary between BCC crystals has  $24 * 24 * 2 = 1152$  equivalent representations. To avoid this ambiguity, the common way of representing a GB is through its disorientation. The disorientation is defined as the misorientation exhibiting the lowest angle  $\theta$  in a given fundamental zone. The usual convention is to select the fundamental zone in which the components of the misorientation axis  $\vec{a}$  obey to the following constraints

$$a_1 \geq a_2 \geq a_3 \geq 0 \quad (4.9)$$

The result of this procedure is the *disorientation*  $D$  transforming a vector representation from the fundamental zone of grain  $A$  to the fundamental zone of grain  $B$ . When computing a GB disorientation it is critical to retain which symmetry operators indexes,  $i, j$ , and which form of Eq. 4.8 were used. Such information are crucial in calculation involving the GB normal.

#### 4.4.2 The tilt and twist angle of a GB

The alignment between the grain boundary normal  $\vec{n}$  and the disorientation axis determines the character of GB. A GB can be classified as a twist boundary, a tilt boundary or mixed. A twist GB has the disorientation axis  $\vec{a}$  perpendicular to the GB plane. A tilt boundary has the disorientation axis  $\vec{a}$  embedded in the GB plane. For all other cases a GB is classified as mixed (e.g. it has both a tilt and a twist component). To compute the tilt and twist angles, the GB normal  $\vec{n}$  needs to be rotated into the disorientation fundamental zone coordinate system. First, one needs to select a reference grain and its outward normal. With the grain selected the appropriate rotation matrix and symmetry operator can be used to rotate the normal in the disorientation fundamental zone. For instance, by selecting grain  $A$  the rotation matrix  $\mathbf{g}_A$  and symmetry operator  $\mathbf{S}_j$  must be used (see Eqs. 4.8 and 4.9). One also need to account if the disorientation results from Eq. 4.8 or its inverse. In the first case Eq. 4.10 must be used to rotate the normal, in the latter 4.11

$$\vec{n}_{A,FZ} = (\mathbf{S}_j \mathbf{g}_A)^T \vec{n}_{A,sample} \quad (4.10)$$

$$\vec{n}_{A,FZ} = (\mathbf{S}_j \mathbf{g}_A) \vec{n}_{A,sample} \quad (4.11)$$

With this crucial step clarified, the tilt and twist angle can be correctly evaluated by using the following methodology [59]. First, one needs to compute the GB normal of grain  $B$  in the fundamental zone. The  $\vec{n}_{B,FZ}$  can be computed by applying the disorientation  $D$  to vector  $\vec{n}_{A,FZ}$  (e.g.  $\vec{n}_{B,FZ} = D\vec{n}_{A,FZ}$ ). The tilt axis  $\vec{T}$  and tilt angle  $\alpha_T$  can be computed by means of Eqs. 4.12 and 4.13

$$\vec{T} = \frac{\vec{n}_{A,FZ} \times \vec{n}_{B,FZ}}{\|\vec{n}_{A,FZ} \times \vec{n}_{B,FZ}\|} \quad (4.12)$$

$$\alpha_T = \sin^{-1} (\|\vec{n}_{A,FZ} \times \vec{n}_{B,FZ}\|) \quad (4.13)$$

The twist axis is by definition the GB normal in the fundamental zone. The twist angle  $\alpha_{TW}$  can be computed using Eq. 4.14

$$\alpha_{TW} = \cos^{-1} \left( 2 \left( \frac{1 + \cos(\theta)}{1 + \cos(\alpha_T)} \right) - 1 \right) \quad (4.14)$$

where  $\theta$  is the disorientation angle defined in Eq. 4.6.

#### 4.4.3 Grain boundary classification

The coincident site lattice (CSL) theory [42] is a well established tool used to predict the structure of GB based upon the density of coincident atoms at a GB interface. The result of CSL theory is a list of GBs classified by their disorientation  $D$  in the form of density of coincident atoms (commonly known as  $\Sigma$ ) and an axis-angle pair describing the disorientation. The value of  $\Sigma$  represents the density of coincident (common) atoms between the lattices of the two grains (e.g. if  $\Sigma = 3$  the two lattice have a common atom at every third lattice site). The disorientation is usually presented in terms of Miller indexes [32] for the axis of rotation. Miller index represents a lattice vector by using only integer components. Miller index notation is useful because it gives a direct representation of lattice directions.

The CSL theory utilizes the discrete nature of atoms and Miller Index notation to generate a list of GB given the axis-angle pair describing the GB disorientation.

#### 4.4.3.1 Generation of the CSL boundary list

The list of CSL boundaries can be generated using the following procedure. The  $\Sigma$  value (see Eq. 4.15) of a CSL GB results from two components: (i) the Miller index of the axis of rotation and (ii) the two co-prime integers ( $n, m$ ).

$$\Sigma(n, m, h, k, l) = n^2 + m^2 \|h^2 + k^2 + l^2\|^2 \quad (4.15)$$

where  $h, k, l$  are the Miller index of the axis of rotation in the fundamental zone (e.g.  $h \geq k \geq l$  and  $h, k, l \geq 0$ ) and the co-prime positive integers  $n, m$ , subject the constraint  $n \geq m$ . The integers  $n, m$  represent the cathetus of the right triangle required to construct the CSL cell assuming the disorientation axis being aligned with  $h, k, l$ . Furthermore, for any cubic lattice,  $\Sigma$  can only be an odd integer number [11]. If the results of Eq. 4.15 is an even number,  $\Sigma$  must be divided by two until an odd number is obtained.

The disorientation angle of CSL boundary is computed using the Eq. 4.16.

$$\theta_{CSL} = 2 \tan^{-1} \left( \frac{m}{n} \|h^2 + k^2 + l^2\| \right) \quad (4.16)$$

The entire list of CSL GBs for cubic crystals cannot be achieved numerically because it would imply ranging an infinite space of integer values. However, an extensive list of CSL GBs for cubic crystals can be obtained using a maximum value of  $n = 10$  and  $h = 100$ .

#### 4.4.3.2 The Brandon criterion for grain boundary classification

A GB can be classified as a CSL GB by utilizing the well established Brandon Criterion [4]. The criterion compares the distance between a GB disorientation  $\mathbf{D}$  to the disorientation of an ideal CSL GB. If such distance is smaller than a certain tolerance, then the GB is a CSL GB.

According to Brandon, the tolerance scales with the  $\Sigma$  value of a CSL GB as follows:

$$\Delta\theta_{max} = \frac{\Delta\theta_0}{\sqrt{\Sigma}} \quad (4.17)$$

where  $\Delta\theta_0$  is a parameter and in common practice is  $15^\circ$ . Because a GB disorientation possesses both an axis and an angle, both of them must have a distance to the known CSL GB smaller than  $\Delta\theta_{max}$  (see Eqs. 4.18 and 4.19)

$$\Delta\theta_{axis} = \cos^{-1} (|\vec{a}_{CSL} \cdot \vec{a}_{GB}|) \leq \Delta\theta_{max} \quad (4.18)$$

$$\Delta\theta_{angle} = \cos^{-1} \|\theta_{CSL} - \theta_{GB}\| \leq \Delta\theta_{max} \quad (4.19)$$

When comparing a GB disorientation against an extensive list of CSL GBs, it might happen that the Brandon criterion is satisfied for multiple different CSL GBs. In such cases the GB is assigned to the closest CSL, which is the CSL exhibiting the lowest  $(\Delta\theta_{axis} + \Delta\theta_{angle})/2$  value.

## 5 Conclusions

This report describes three extensions of a physically-based CPFEM model for the creep and creep-rupture properties of Grade 91 steel:

1. Progress on transitioning the modeling framework to the MOOSE finite element package to incorporate multiphysics models and improve parallel scalability.
2. A physically-based method for scaling the model parameters to capture temperature-dependent creep in the expected use temperature range of Grade 91 in SFRs.
3. Incorporating the effect of GB crystallography on the model properties to more accurately capture the effect of microstructural variations.

With these extensions the physically-based model for Grade 91 base material can be regarded as complete. The model captures all the microstructural mechanisms and statistical microstructural variations thought to influence creep in the alloy. The final model can be used to make predictions of engineering properties through the entire temperature range the material is expected to see in service in SFRs.

Most challenges associated with Grade 91 in service in fossil fuel electrical generating facilities relate to welds, not the base material. Future work could begin with this modeling framework and extend it to examine a complete weldment, including base, heat affected zone, and weld material. This will require much larger simulations than those used to determine bulk material properties and additionally will require model development related to accurately capturing the properties of the material in the heat affected zone. Additionally, the modeling framework can be used to look at new high temperature structural materials. With sufficient confidence in the model it could be used to reduce the number of tests and therefore the time required to qualify new materials.



## **Acknowledgments**

The research was sponsored by the U.S. Department of Energy, under Contract No. DE-AC02-06CH11357 with Argonne National Laboratory, managed and operated by UChicago Argonne LLC. Programmatic direction was provided by the Office of Nuclear Energy.

The authors gratefully acknowledge the support provided by Alice Caponiti, Director, Office of Advanced Reactor Technologies (ART), Sue Lesica, Federal Manager, ART Advanced Materials Program, and Robert Hill of ANL, National Technical Director, ART Fast Reactors Campaign.



## Bibliography

- [1] H. B. Aaron and G. F. Bolling. Free volume as a criterion for grain boundary models. *Surface Science*, 31(C):27–49, 1972.
- [2] H. B. Aaron and G. F. Bolling. Free volume as a guide to grain boundary phenomena. *Scripta Metallurgica*, 6(7):553–562, 1972.
- [3] American Society of Mechanical Engineers. Section II, Part D (Metric). In *ASME Boiler and Pressure Vessel Code*. 2015.
- [4] DG Brandon. The structure of high-angle grain boundaries. *Acta metallurgica*, 14(11):1479–1484, 1966.
- [5] Fuhua Cao, Yong Jiang, Tao Hu, and Dengfeng Yin. Correlation of grain boundary extra free volume with vacancy and solute segregation at grain boundaries: a case study for Al. *Philosophical Magazine*, 98(6):464–483, 2018.
- [6] I Chant and KL Murty. Structural materials issues for the next generation fission reactors. *JOM*, 62(9):67–74, 2010.
- [7] B. K. Choudhary and E. Isaac Samuel. Creep behaviour of modified 9Cr-1Mo ferritic steel. *Journal of Nuclear Materials*, 412(1):82–89, 2011.
- [8] FW Crossman and MF Ashby. The non-uniform flow of polycrystals by grain-boundary sliding accommodated by power-law creep. *Acta Metallurgica*, 23(4):425–440, 1975.
- [9] R. H. Dodds, T. J. Truster, K. B. Cochran, D. M. Parks, and T.-L. Sham. Modeling of Creep Deformation and Fracture of Grade 91 Steel through Crystal Plasticity and Grain Boundary Cavitation. Technical report, Argonne National Laboratory, 2016.
- [10] P. S. Follansbee and U. F Kocks. A constitutive description of the deformation of copper based on the use of the mechanical threshold stress as an internal state variable. *Acta Metallurgica*, 36:82–93, 1988.
- [11] Georges Friedel. *Leçons de cristallographie professées à la Faculté des sciences de Strasbourg*. Berger-Levrault, 1926.
- [12] Harold J Frost and Michael F Ashby. *Deformation mechanism maps: the plasticity and creep of metals and ceramics*. Pergamon press, 1982.
- [13] Derek Gaston, Chris Newman, Glen Hansen, and Damien Lebrun-Grandie. MOOSE: a parallel computational framework for coupled systems of nonlinear equations. *Nuclear Engineering and Design*, 239(10):1768–1778, 2009.
- [14] RC Gifkins and KU Snowden. Mechanism for viscous grain-boundary sliding. *Nature*, 212(5065):916, 1966.
- [15] C Goux. Structure des joints de grains: considérations cristallographiques et méthodes de calcul des structures. *Canadian Metallurgical Quarterly*, 13(1):9–31, 1974.

- [16] W. Z. Han, M. J. Demkowicz, E. G. Fu, Y. Q. Wang, and A. Misra. Effect of grain boundary character on sink efficiency. *Acta Materialia*, 60(18):6341–6351, 2012.
- [17] Takanori Hirose, Takashi Nozawa, Roger E Stoller, Dai Hamaguchi, Hideo Sakasegawa, Hiroyasu Tanigawa, Hisashi Tanigawa, Mikio Enoda, Yutai Katoh, and Lance Lewis Snead. Physical properties of F82H for fusion blanket design. *Fusion Engineering and Design*, 89(7-8):1595–1599, 2014.
- [18] Eric R. Homer, Srikanth Patala, and Jonathan L. Priedeman. Grain Boundary Plane Orientation Fundamental Zones and Structure-Property Relationships. *Scientific Reports*, 5:15476, 2015.
- [19] K. Kimura, H. Kushima, and K. Sawada. Long-term creep deformation property of modified 9Cr-1Mo steel. *Materials Science and Engineering A*, 510-511(C):58–63, 2009.
- [20] B. S. Kirk, J. W. Peterson, R. H. Stogner, and G. F. Carey. libMesh: A C++ library for parallel adaptive mesh refinement/coarsening simulations. *Engineering with Computers*, 22(3–4):237–254, 2006. <http://dx.doi.org/10.1007/s00366-006-0049-3>.
- [21] U. F. Kocks. The relation between polycrystal deformation and single-crystal deformation. *Metallurgical and Materials Transactions*, 1(5):1121–1143, 1970.
- [22] U F Kocks. Realistic constitutive relation for metal plasticity. *Materials Science and Engineering A*, 317:181–187, 2001.
- [23] U. F. Kocks, A. S. Argon, and M. F. Ashby. Thermodynamics and kinetics of slip. In B. Chalmers, J. W. Christian, and T. B. Massalski, editors, *Progress in Materials Science*, pages 64–291. 1975.
- [24] J Koike, R Ohyama, T Kobayashi, M Suzuki, and K Maruyama. Grain-boundary sliding in AZ31 magnesium alloys at room temperature to 523 K. *Materials Transactions*, 44(4):445–451, 2003.
- [25] S. Kok, A. J. Beaudoin, and D. A. Tortorelli. A polycrystal plasticity model based on the mechanical threshold. *International Journal of Plasticity*, 18(5-6):715–741, oct 2002.
- [26] TG Langdon. A unified approach to grain boundary sliding in creep and superplasticity. *Acta Metallurgica et Materialia*, 42(7):2437–2443, 1994.
- [27] F. R. Larson and J. Miller. A time-temperature relationship for rupture and creep stresses. *Transactions of the ASME*, 74:765–771, 1952.
- [28] J K Mackenzie. Second paper on statistics associated with the random disorientation of cubes. *Biometrika*, 45(1-2):229–240, 1958.
- [29] Kouichi Maruyama, Junya Nakamura, Kyosuke Yoshimi, and Yuji Nagae. Evaluation of long-term creep rupture life of Gr.91 steel by analysis of on-going creep curves. In *Proceedings from the Eighth International Conference on Advances in Materials Technology for Fossil Power Plants*, pages 467–478, 2016.

- [30] H Mecking, B Nicklas, N. Zarubova, and U F Kocks. A “universal” temperature scale for plastic flow. *Acta Metallurgica*, 34(3):527–535, 1986.
- [31] M. C. Messner, T. J. Truster, K. B. Cochran, D. M. Parks, and T.-L. Sham. FY17 status report on the micromechanical finite element modeling of creep fracture of Grade 91 steel. Technical Report ANL-ART-95, Argonne National Laboratory, 2017.
- [32] William Hallowes Miller. *A treatise on crystallography*. For J. & JJ Deighton, 1839.
- [33] A. Morawiec, J. A. Szpunar, and D. C. Hinz. Texture influence on the frequency of occurrence of CSL-boundaries in polycrystalline materials. *Acta Metallurgica Et Materialia*, 41(10):2825–2832, 1993.
- [34] Marie-Hélène Nadal and Philippe Le Poac. Continuous model for the shear modulus as a function of pressure and temperature up to the melting point: analysis and ultrasonic validation. *Journal of applied physics*, 93(5):2472–2480, 2003.
- [35] A. Needleman and J. R. Rice. Plastic Creep Flow Effects in the Diffusive Cavitation of Grain Boundaries. *Acta Metallurgica*, 28(10):1315–1332, 1980.
- [36] Vinh Phu Nguyen. An open source program to generate zero-thickness cohesive interface elements. *Advances in Engineering Software*, 74:27–39, 2014.
- [37] David L. Olmsted, Stephen M. Foiles, and Elizabeth A. Holm. Survey of computed grain boundary properties in face-centered cubic metals: I. Grain boundary energy. *Acta Materialia*, 57(13):3694–3703, 2009.
- [38] David L. Olmsted, Elizabeth A. Holm, and Stephen M. Foiles. Survey of computed grain boundary properties in face-centered cubic metals-II: Grain boundary mobility. *Acta Materialia*, 57(13):3704–3713, 2009.
- [39] Srikanth Patala and Christopher A. Schuh. Symmetries in the representation of grain boundary-plane distributions. *Philosophical Magazine*, 93(5):524–573, 2013.
- [40] Chao Pu, Yanfei Gao, Yanli Wang, and T. L. Sham. Diffusion-coupled cohesive interface simulations of stress corrosion intergranular cracking in polycrystalline materials. *Acta Materialia*, 136:21–31, 2017.
- [41] R Raj and MF Ashby. On grain boundary sliding and diffusional creep. *Metallurgical transactions*, 2(4):1113–1127, 1971.
- [42] S. Ranganathan. On the geometry of coincidence-site lattices. *Acta Crystallographica*, 21(2):197–199, aug 1966.
- [43] Sutatch Ratanaphan, David L. Olmsted, Vasily V. Bulatov, Elizabeth A. Holm, Anthony D. Rollett, and Gregory S. Rohrer. Grain boundary energies in body-centered cubic metals. *Acta Materialia*, 88:346–354, 2015.
- [44] Mohsen Khajeh Salehani and Nilgoon Irani. A coupled mixed-mode cohesive zone model: An extension to three-dimensional contact problems. *arxiv.org*, jan 2018.

- [45] T. L. Sham and A. Needleman. Effects of triaxial stressing on creep cavitation of grain boundaries. *Acta Metallurgica*, 31(6):919–926, 1983.
- [46] L. S. Shvindlerman, G. Gottstein, V. A. Ivanov, D. A. Molodov, D. Kolesnikov, and W. Łojkowski. Grain boundary excess free volumedirect thermodynamic measurement. *Journal of Materials Science*, 41(23):7725–7729, 2006.
- [47] VK Sikka. Modified 9Cr-1Mo steel-an improved alloy for steam generator application. *Ferritic Steels for High Temperature Applications*, 65, 1983.
- [48] D. J. Steinberg, S. G. Cochran, and M. W. Guinan. A constitutive model for metals applicable at high-strain rate. *Journal of Applied Physics*, 51(3):1498–1504, 1980.
- [49] R. W. Swindeman. Cyclic Stress-Strain-Time Response of a 9Cr-1Mo-V-Nb Pressure Vessel Steel at High Temperature. In H. D. Solomon, G. R. Halford, L. R. Kaisand, and B. N. Leis, editors, *Low Cycle Fatigue, ASTM STP 942*, pages 107–122. American Society for Testing and Materials, Philadelphia, 1988.
- [50] R. W. Swindeman. Construction of isochronous stress-strain curves for 9Cr-1Mo-V Steel. *Advances in Life Prediction Methodology*, 391:95–100, 1999.
- [51] RW Swindeman, ML Santella, PJ Maziasz, BW Roberts, and K Coleman. Issues in replacing Cr–Mo steels and stainless steels with 9Cr–1Mo–V steel. *International Journal of Pressure Vessels and Piping*, 81(6):507–512, 2004.
- [52] Yukio Takahashi. Study on creep-fatigue evaluation procedures for high-chromium steels Part I: test results and life prediction based on measured stress relaxation. *International Journal of Pressure Vessels and Piping*, 85(6):406–422, 2008.
- [53] M. A. Tschopp and D. L. McDowell. Structures and energies of 3 asymmetric tilt grain boundaries in copper and aluminium. *Philosophical Magazine*, 87(22):3147–3173, 2007.
- [54] M. A. Tschopp, K. N. Solanki, F. Gao, X. Sun, M. A. Khaleel, and M. F. Horstemeyer. Probing grain boundary sink strength at the nanoscale: Energetics and length scales of vacancy and interstitial absorption by grain boundaries in  $\alpha$ -Fe. *Physical Review B - Condensed Matter and Materials Physics*, 85(6):1–21, 2012.
- [55] Viggo Tvergaard. Analysis of creep crack growth by grain boundary cavitation. *International Journal of Fracture*, 31(3):183–209, 1986.
- [56] D. Wolf. Correlation between the energy and structure of grain boundaries in b.c.c. metals: I. Symmetrical boundaries on the (110) and (100) planes. *Philosophical Magazine B: Physics of Condensed Matter; Statistical Mechanics, Electronic, Optical and Magnetic Properties*, 59(6):667–680, 1989.
- [57] D. Wolf. Correlation between energy and volume expansion for grain boundaries in fcc metals. *Scripta Metall.*, 23(11):1913–1918, 1989.

- [58] D. Wolf. Correlation between the energy and structure of grain boundaries in b.c.c. metals. II. Symmetrical tilt boundaries. *Philosophical Magazine A: Physics of Condensed Matter, Structure, Defects and Mechanical Properties*, 62(4):447–464, 1990.
- [59] D Wolf and J F Lutsko. On the Geometrical Relationship Between Tilt and Twist Grain-Boundaries. *Zeitschrift Fur Kristallographie*, 189:239–262, 1989.
- [60] Masatsugu Yaguchi and Yukio Takahashi. Ratchetting of viscoplastic material with cyclic softening, part 2: application of constitutive models. *International Journal of Plasticity*, 21:835–860, 2005.



## Distribution List

<i>Name</i>	<i>Affiliation</i>	<i>Email</i>
Caponiti, A.	DOE	alice.caponiti@nuclear.energy.gov
Gouger, H.D.	INL	hans.gougar@inl.gov
Grandy, C.	ANL	cgrandy@anl.gov
Hill, R.N.	ANL	bobhill@anl.gov
Krumdick, G.K.	ANL	gkrumdick@anl.gov
Lesica, S.	DOE	sue.lesica@nuclear.energy.gov
Li, M.	ANL	mli@anl.gov
McMurtrey, M.	INL	michael.mcmurtrey@inl.gov
Messner, M.C.	ANL	messner@anl.gov
Natesan, K.	ANL	natesan@anl.gov
Qualls, A.L.	ORNL	quallsal@ornl.gov
Sham, T.-L.	ANL	ssham@anl.gov
Singh, D.	ANL	dsingh@anl.gov
Sowinski, T.E.	DOE	thomas.sowinski@nuclear.energy.gov
Wang, H.	ORNL	wangh@ornl.gov
Wang, Y.	ORNL	wangy2@ornl.gov
Wright, R.	INL	richard.wright@inl.gov
Zhang, X.	ANL	xuanzhang@anl.gov







## **Applied Materials Division**

Argonne National Laboratory  
9700 South Cass Avenue, Bldg. 208  
Argonne, IL 60439

[www.anl.gov](http://www.anl.gov)



Argonne National Laboratory is a U.S. Department of Energy  
laboratory managed by UChicago Argonne, LLC